

Insights into the mechanics of pure and bacteria-laden sessile whole blood droplet evaporation

Durbar Roy^{1,†}, Sophia M. Joseph^{2,†}, Kush Kumar Dewaangan², Abdur Rasheed², Siddhant Jain², Anmol Singh³, Dipshikha Chakravortty³ and Saptarshi Basu²

(Received 18 October 2024; revised 15 August 2025; accepted 15 September 2025)

We study the mechanics of evaporation and precipitate formation in pure and bacterialaden sessile whole blood droplets in the context of disease diagnostics. Using experimental and theoretical analysis, we show that the evaporation process has three stages based on evaporation rate. In the first stage, edge evaporation results in a gelated contact line along the periphery through a sol-gel phase transition. The intermediate stage consists of a gelated front propagating radially inwards due to capillary flow and droplet height regression in pinned mode, forming a wet-gel phase. We unearthed that the gelation of the entire droplet occurs in the second stage, and the wet-gel formed contains trace amounts of water. In the final slowest stage, the wet gel transforms into a dry gel, leading to desiccation-induced stress forming diverse crack patterns in the precipitate. Slow evaporation in the final stage is quantitatively measured using evaporation of trace water and associated transient delamination of the precipitate. Using the axisymmetric lubrication approximation, we compute the transient droplet height profile and the erythrocytes concentration for the first two stages of evaporation. We show that the precipitate thickness profile computed from the theoretical analysis conforms to the optical profilometry measurements. We show that the drop evaporation rate and final dried residue pattern do not change appreciably within the parameter variation of the bacterial concentration typically found in bacterial infection of living organisms. However,

¹International Centre for Theoretical Sciences, Tata Institute of Fundamental Research, Bengaluru 560089, India

²Department of Mechanical Engineering, Indian Institute of Science, Bengaluru 560012, India

³Department of Microbiology and Cell Biology, Indian Institute of Science, Bengaluru 560012, India **Corresponding author:** Saptarshi Basu, sbasu@iisc.ac.in

[†]Durbar Roy and Sophia M. Joseph contributed equally to this work.

at exceedingly high bacterial concentrations, the cracks formed in the coronal region deviate from the typical radial cracks found in lower concentrations.

Key words: drops and bubbles

1. Introduction

In this study, we investigate the mechanics of sessile droplet evaporation in pure and bacteria-laden blood droplets. Understanding the behaviour of blood droplet evaporation is essential in forensic science, biotechnology and the development of advanced medical diagnostics (Brutin 2015; Chen et al. 2016; Brutin & Starov 2018; Cameron et al. 2018; Kokornaczyk, Bodrova & Baumgartner 2021; Pal et al. 2020, 2021, 2023; Seyfert et al. 2022; Demir et al. 2024; Brutin & Sefiane 2022). In particular, forensic investigators routinely use blood stain and blood splatter pattern analysis to recreate and understand a crime scene in exclusive detail (Hulse-Smith, Mehdizadeh & Chandra 2005; Benabdelhalim & Brutin 2022). Blood splatter and corresponding stains are caused due to a myriad of blood droplets impinging various surfaces and interfaces (Yarin, Roisman & Tropea 2017; Roy et al. 2019, 2022, 2023). At equilibrium, blood drops and films become sessile, and subsequent evaporation leads to residues which forms the basis of forensic investigation. The mechanics of drop impact (Yarin et al. 2017) and evaporation of thin films/drops (Sultan, Boudaoud & Amar 2005; Brutin 2015) becomes important for such forensic investigations in general. We also observe evaporation in various biological and bodily fluids like blood clots, desiccation in wounds (Brutin et al. 2011; Sobac & Brutin 2011; Laux, Ferrandis & Brutin 2016), biofilm formations (Wilking et al. 2013) and drying of tears (Traipe-Castro et al. 2014; Roy & Basu 2024), to name a few that are found in living systems. Apart from forensics and disease diagnostics, analysis of desiccated biological samples is essential in several applications like archaeological studies (Kooyman, Newman & Ceri 1992; Wilson et al. 2013), micro-array applications for proteins, nucleic acids (DNA, RNA), and genotype and phenotype studies (Blossey & Bosio 2002; Dugas et al. 2005; Smalyukh et al. 2006). Analysing the characteristics of sessile blood droplets during and after evaporation can provide valuable insights into the blood sample's source, age and composition. The physics of sessile blood drop evaporation falls at the intersection of various disciplines like fluid mechanics, solid mechanics, soft matter, statistical physics, surface chemistry, colloidal physics and biology, to name a few (Brutin 2015); and as a result, quantitative understanding of blood droplet evaporation and its corresponding precipitate formation mechanics still remains in its infancy (Lanotte et al. 2017).

Blood is a complex naturally occurring fluid consisting of formed cellular elements suspended in blood plasma and is found in all humans and complex animal species (Baskurt & Meiselman 2003; Hoffbrand & Steensma 2019). Various cellular elements like the biconcave (at rest) erythrocytes (red blood cells; RBCs), formless leukocytes (white blood cells; WBCs) and disc shaped thrombocytes (platelets) form approximately 45 %–50 % of the blood volume, with RBCs having the most significant percentage among the cellular elements. However, blood plasma is an amber colour liquid component of the blood, which makes approximately 50 %–55 % of the total blood volume. Subsequently, 94 %–95 % of the blood plasma by volume is essentially water, with the remaining 5 %–6 % being dissolved proteins (fibrinogen, albumin), electrolytes, glucose, clotting factors, hormones, carbon dioxide and oxygen. As discussed previously, blood is a highly

concentrated colloidal suspension and its concentration is usually described by the volume fraction/haematocrit (Ht). For healthy individuals, the physiological range of haematocrit is $Ht \approx 40\,\%-45\,\%$ (Reinhart 2016). The very high concentration of RBCs makes optical diagnostics of evaporating blood droplets challenging in general. Based on volume ratio, blood can be thought of as comprising two major components, RBCs ($V_{RBCs}/V \approx 40\,\%-45\,\%$) and plasma ($V_{plasma}/V \approx 55\,\%-60\,\%$) where V_{RBCs} , V_{plasma} represents the respective volumes in a total blood volume V. We can, therefore, approximate blood as a colloidal suspension (Israelachvili 2011) of RBCs in plasma to first-order accuracy. The morphology of dried residues of blood drops hence depends primarily on the deposition of RBCs, the major solute component of blood plasma. However, other cellular components of blood (leukocytes and thrombocytes), dissolved proteins, electrolytes, hormones and gases have a secondary role in the dried residue pattern formation. Such secondary effects are essential in developing diagnostic solutions for particular diseases in general (Chen et al. 2016; Kokornaczyk et al. 2021). However, in this work, we focus primarily on the deposit pattern caused by RBCs.

Evaporation of biofluids like blood, saliva, mucus and urine has been explored majorly in sessile droplet and thin film configurations on solid substrates due to the simplicity of the experimental set-up (Hu & Larson 2002, 2005; Brutin 2015; Kokornaczyk et al. 2021; Wilson & D'Ambrosio 2023). The major observations for sessile blood droplet evaporation were the formation of a ring-like deposit at the contact line and a complex set of crack patterns in the desiccated drops and films. The different patterns formed in evaporating drops and films of biological fluids resembled patterns found in various colloidal systems hinting towards some unifying underlying laws that were common to biofluids, colloids and pure fluids in general (Denkov et al. 1992; Adachi, Dimitrov & Nagayama 1995; Deegan et al. 1997, 2000; Allain & Limat 1995; Dufresne et al. 2003; Bhardwaj et al. 2009, 2010; Tarasevich, Vodolazskaya & Isakova 2011; Stauber et al. 2014; Kaplan & Mahadevan 2015; Chen et al. 2016). Previous studies by scientists and engineers using model fluids like mucin revealed that both deposition and crack formation depends strongly on the particle concentration and types of dissolved salts, macro-molecules, proteins and surfactants (Nguyen & Stebe 2002). This work explores blood drop evaporation physics in depth and also tests whether microbial bacteria present in blood simulating bacterial infection found in living organisms can affect the evaporation process and the resulting dried precipitate.

It has been shown by various research groups (Shatokhina 2004; Yakhno et al. 2005; Esmonde-White et al. 2014; Kokornaczyk et al. 2021) that pathological changes of solute and solvent composition affect the morphology of the dried residues in evaporating drops and films. Up to the recent decade, desiccation studies on biological fluids have majorly focused on solutions, but the evaporation physics of drying suspensions is relatively sparse and qualitative in nature. Some of the recent seminal work of Brutin et al. (2011), Chen et al. (2016) and Pal et al. (2020, 2021, 2023) being an exception. Brutin and his collaborators (2011) analysed the blood drop evaporation mechanism, desiccation time and dried precipitate morphology using optical diagnostics and mass measurements. Further, Brutin et al. (2011) provided five stages of blood droplet evaporation based on qualitatively observed features. The stage classification was chosen based on visual cue and hence lacked key quantitative insights. In principle, the stages can be reduced into fewer stages (2–3) based on quantitative data, as was shown by Sobac & Brutin (2011). Sobac & Brutin (2011) showed that the blood droplet evaporation can be divided into two major stages overlapping with a transition stage, which essentially makes it a three stage process, and the current work follows similar reasoning.

In this work, we follow a similar three-stage classification based on quantitative droplet regression data. In the present work, the major stages naturally emerge and can be uniquely determined from the normalised droplet volume regression curve (refer to figure 2b). The first stage of evaporation (stage A) ends when the evaporation curves deviate from the initial linear evolution. The end of second stage and the transition regime encompasses the second stage (stage B), and the final stage (stage C) represents the final and very slow evaporation rate, where processes like major crack formation and precipitate delamination occur. Although the work of Brutin et al. is highly important as it outlines the essential physics, there exist some fundamental shortcomings related to the mechanistic understanding of the underlying processes involved. One important example being the cause of the internal flow generated during the evaporation of blood droplets. Brutin et al. (2011) reason that the internal flow is due to Marangoni effects owing to the small value of Reynolds, capillary and Rouse numbers. However, as was shown later (Chen et al. 2016; Lanotte et al. 2017; Iqbal, Shen & Sen 2020), the internal flow generated during evaporation is essentially capillary flow, which produces a coffee ring kind of deposition in pure/dilute colloidal solutions/suspensions as was shown by the seminal work of Deegan et al. (1997, 2000). Further, the circular spots at the end of evaporation was associated with drying spots by Brutin et al. (2011); however, as was conjectured later by Sobac & Brutin (2014), the circular spots essentially indicates laminated regions (regions that have relatively higher water content) and surrounding delaminated regions. Recently, in a series of work, Pal et al. (2020, 2021, 2023) provided important insights related to phase transition and the role of blood proteins on the precipitate pattern in dilute blood solutions. The majority of previous studies (Chen et al. 2016; Lanotte et al. 2017; Iqbal et al. 2020; Pal et al. 2020, 2021, 2023; Du, Zhang & Shen 2022) are based on diluted blood solution; however, there is a need to investigate whole blood droplet evaporation from a mechanistic perspective to test the feasibility of various blood precipitate bio-markers as diagnostic tools (Trantum, Wright & Haselton 2012; Chen et al. 2016). Further, owing to a very high Ht, investigating whole blood droplet evaporation is challenging both experimentally (Bodiguel & Leng 2010; Lanotte et al. 2017) and theoretically. We therefore observe that there is a need for a better mechanistic and quantitative measurement/understanding of the various processes that occur during whole blood droplet evaporation in the context of various disease diagnostic.

The current work studies blood droplet evaporation and provides insights into the physics of evaporation and precipitate formation in bacteria-laden whole blood droplets using high fidelity optical diagnostics and theoretical analysis. We also investigate the effect of bacterial concentration on evaporation, precipitate and crack formation. The spatio-temporal evaporation and precipitate dynamics in first two stages (A, B) is modelled through coupling between evaporation flux, droplet height and RBCs concentration from first principles using axisymmetric lubrication model. Further, the droplet precipitate is studied using micro/nano characterisation techniques like profilometry, scanning electron microscopy (SEM) and optical microscopy that provides additional quantitative insights into the physics of precipitate formation and RBC distribution. The wet gel to dry gel transition during the very slow stage C of evaporation is measured quantitatively using trace water evaporation and precipitate delamination dynamics. The bacterial motion and distribution is further mapped using live fluorescence confocal microscopy. In general, the evaporation and the dried residue of a desiccating biological fluid such as blood depend on the ambient environmental factors (like temperature and humidity), substrate characteristics (like chemical composition, wettability, adhesion), droplet geometry, and fluid mechanical (like density, viscosity, surface tension, pathology), physicochemical, thermofluidic and biophysical properties. The dried blood drop dominant pattern consists

of a thick rim called a corona and a centre region of relatively small thickness. The coronal rim thickness is caused due to the transport of RBCs by capillary flow induced by sessile drop evaporation (Sobac & Brutin 2011, 2014; Brutin 2015; Chen et al. 2016; Hertaeg et al. 2021). The interaction of desiccation-induced stress and thickness variation from the drop centre to the outer rim region in the radial direction causes crack patterns of different morphologies. Radial cracks are formed in the rim region, whereas mud-flat cracks are formed in the centre and outer periphery of the dried residues. Evaporating colloidal and polymeric sessile drops analogously form a skin layer at the air-liquid interface, which eventually undergoes a buckling. Current literature on blood drop evaporation is primarily based on observational characteristics of drop shape, mass and crack patterns (Bahmani, Neysari & Maleki 2017; Choi, Kim & Kim 2020; Iqbal et al. 2020; Mukhopadhyay et al. 2020; Hertaeg et al. 2021). However, a fundamental mechanistic understanding of the blood drop desiccation process is far from complete and requires thorough quantitative analysis. This work serves as a bridge to understand the mechanics of blood drop evaporation using ideas from colloidal desiccating drops. We decipher the various stages and the allied mechanisms of blood drop drying using high-fidelity colour optical imaging, quantitative theoretical modelling and experimental micro/nano-characterisation. It is important to note that the current work establishes the mechanics/mechanisms of the various processes and stages related to blood droplet drying and precipitate formation physics in evaporating pure and bacteria-laden sessile blood droplets in a quantitative manner using experimental and theoretical methods. The detailed experimental characterisation of various physical parameter ranges is outside the scope of the present work. Further, to the best of our knowledge, this study is the first of its kind to study the effect of bacteria on evaporation and precipitate formation in sessile droplets in a comprehensive manner using both experimental and theoretical methods. It is important to note that the theoretical framework developed in this work is based on the scaling of the governing conservation laws and the corresponding experimental data. The motivation of the theoretical framework was to establish the time varying droplet thickness profile, final precipitate deposit profile, RBCs concentration, gelation front propagation, and a physical understanding of the crack size and flake size based on the precipitate thickness characteristics. The exact analytical or numerical solutions of the fully coupled unsteady three-dimensional (3-D) governing equations of mass, momentum, energy and concentration is outside the scope of the present study. The authors want to highlight that the current manuscript comprehensively investigates the coupled evaporation-precipitation mechanics and the various stages of bacterialaden sessile whole blood droplet evaporation from rigorous first principles using both experimental and theoretical analysis, which does not exist in the literature according to the authors knowledge. In particular, theoretical prediction and subsequent agreement with experimental data for blood droplet evaporation and precipitate height profile has not been reported in the literature.

The current manuscript is structured as follows. Section 2 discusses the materials and methods in several subsections. Blood sample preparation, experimental set-up and dried residue characterisation are discussed in §§ 2.1, 2.2 and 2.3, respectively. Section 3.1 introduces the key results as a global overview. Section 3.2 discusses the coordinate system used and sessile droplet evaporation physics. Section 3.3 discusses the various stages of blood drop evaporation. Section 3.4 discusses the quantitative modelling and the generalised mechanics of blood drop evaporation. Section 3.5 presents the characterisation of dried blood residues, discusses the cracking mechanics due to desiccation stresses, bacterial distribution and the role of bacterial concentration on the precipitate crack patterns. Section 4 concludes the manuscript.

2. Materials and methods

2.1. Blood sample preparation

Blood samples were collected from three healthy volunteers (one female and two male) in the age group range (25-40 years) with proper consent. First, 10 ml of whole blood was drawn in K3-EDTA (tripotassium Ethylene Diamine Tetraacetic Acid) vacutainer containers to prevent the blood from clotting. Then, 2-4 ml of the collected blood were sent for several blood tests (CBC, Complete Blood Count; PT, Prothrombin Time; and ESR, Erythrocyte Sedimentation Rate; refer to supplementary table ST1 for relevant blood report data) relevant to the mechanics of the various processes that occur during evaporation. Overnight-grown stationary phase cultures of Klebsiella pneumoniae MH1698 were taken, and their absorbance was measured at OD600 nm. Various bacterial concentrations of 10⁶, 10⁹, 10¹² CFU ml⁻¹ of the bacterial culture were pelleted down at 6000 rpm for 6 min. CFU (colony forming units) is a measure of the number of viable microbial cells in a sample. The bacterial concentration parameter was varied over three orders of magnitude to ensure sufficient separation in the concentration parameter space and to avoid overlap due to experimental uncertainty. The pellets were washed twice with phosphate-buffered saline (PBS) pH 7.4 and resuspended in EDTA whole blood. For confocal microscopy studies, S. typhimurium expressing green fluorescent protein (GFP) (pFV-GFP) (STM-GFP) strains were used. Bacterial concentration larger than 10¹² CFU ml⁻¹ becomes infeasible in our current experiments due to the very large requirement of raw culture of bacterial solution that is diluted repeatedly to attain the desired bacterial concentration. Further, raw bacterial solution concentration higher than 10¹² CFU ml⁻¹ becomes very muddy and viscous, which makes handling the samples difficult using typical fluid handling equipment like micro-pipettes and syringes. Viscosity measurements of the samples were performed using cone-and-plate geometry (plate diameter, 40 mm; cone angle, 1°) of a commercial rheometer (Anton Paar, model MCR302).

2.2. Experimental set-up

Figure 1 shows a schematic representation of the experimental set-up. The experimental set-up consists of a blood drop evaporating on a clean glass slide of dimensions 75 × $25 \times 1 \text{ mm}^3$ (procured from Blue Star). Blood droplet with a volume of $3.4 \pm 0.8 \,\mu\text{l}$ was placed gently on the glass slide using a micro-pipette. All the evaporation experiments were performed at a relative humidity (RH) of 45 % \pm 3 % and an ambient temperature of 25 ± 2 °C measured using a TSP-01 sensor, Thorlabs. The complete evaporation process is recorded using colour optical diagnostics from three views, i.e. top, side and bottom. The top and bottom views were operated in reflection mode, whereas shadowgraphy was performed using side-view imaging. Colour images of the corresponding views (top, bottom and side) were recorded using three DSLR cameras with an image resolution of 24 megapixels (Nikon D5600) coupled with Navitar zoom lens assembly (2X lens × 4X adapter tube). A 5W LED light source (Holmarc) and a 50W mercury lamp were used to provide uniform illumination for the three imaging views. A spatial resolution of 1 µm pixel⁻¹ was used for the optical colour imaging. Consecutive images were captured at a time delay of 10 s. Typical sample top, side and bottom view images are shown in figure 1 (refer to supplementary movies for temporal data of drop evaporation). The scale bar in white denotes 1 mm. Sufficient number (a minimum of 10 trials are conducted for each experimental parameter) of experimental runs were conducted to ensure a statistical significant dataset. The instantaneous geometrical parameters and features (shape descriptors) are extracted using image processing techniques applied to the side, top and bottom view images using open source software ImageJ (Schneider,

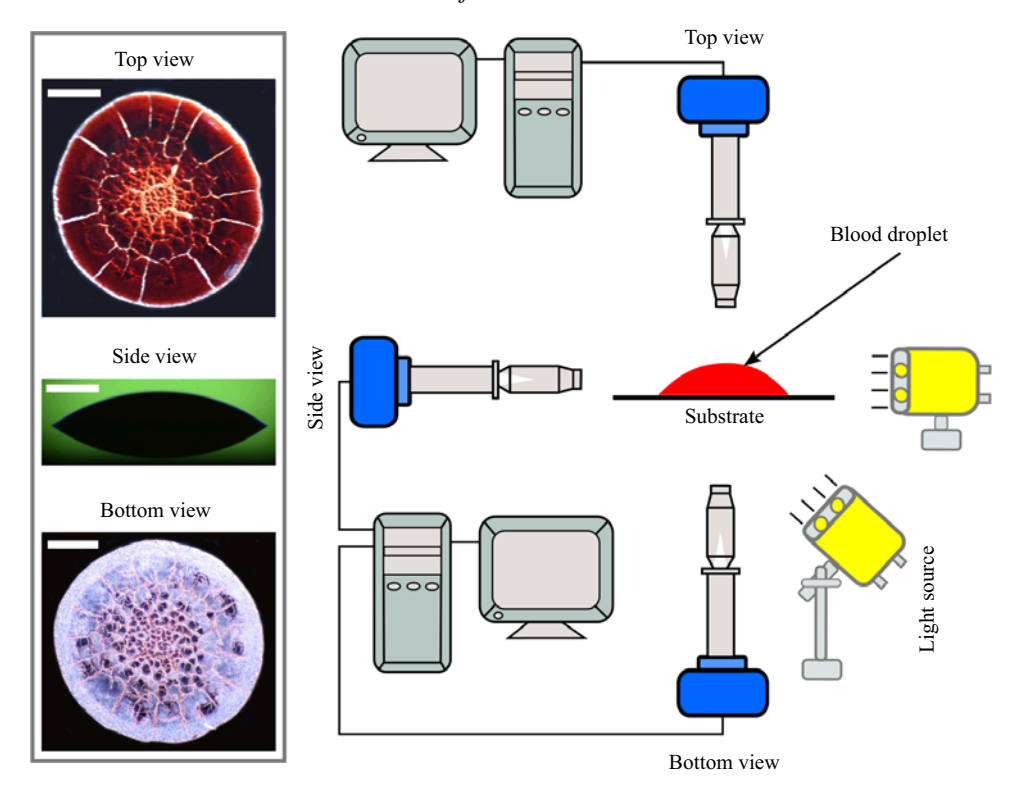


Figure 1. Schematic of the experimental set-up, and sample top, side and bottom view images of dried blood drop precipitate. Scale bar depicted in white represents 1 mm.

Rasband & Eliceiri 2012) and python programming language (Van Rossum & Drake 2009).

The water content and the delamination height were computed from the reflected light received on the bottom DSLR. The change in colour in the third stage of evaporation occurs due to the loss of water and its corresponding delamination height. In general, the delamination height is inversely proportional to the water content in the precipitate. To quantify our measurements in arbitrary intensity units, we map the delamination height to the reciprocal of the water content intensity distribution. The white light image was decomposed into its constituent RGB spectrum/modes and the strongest energy component (blue for the bottom) was used. The intensity range of $[0, 2^8 - 1]$ was mapped to a floating point intensity range [0, 1] before further processing. The intensity signals were then thresholded and segmented to remove outlier intensity signals. The entire resolution of the image was used to generate a interpolated intensity signal and the corresponding images were smoothed using appropriate bandpass filters. The filtered image was remapped to the $[0, 2^8 - 1]$ intensity range and the resultant image was passed through the contrast limited adaptive histogram equalisation (CLAHE) function. The image output was then calibrated with respect to the non-dimensional time 0.67 where everywhere, the height was assigned zero as the corresponding intensity was zero except the outer edge of the droplet, where the intensity was non-zero at certain places due to delamination. The delamination height and water content were hence measured with respect to a certain temporal instant. It is important to note that the above-described procedure is a relative method and does not correspond to absolute measurements.

D. Roy and others

All statistical analysis, data visualisation and numerical computation were done using in-house codes in python (Van Rossum & Drake 2009).

2.3. Dried residue characterisation and bacterial distribution

Scanning electron microscopy (SEM) was employed to analyse the surface characteristics of the deposits, revealing the microcrack patterns through high-resolution imaging. An Ultra55 FE- SEM Karl Zeiss EDS instrument is used. SEM images showed the detailed crack patterns and stacking of RBCs on the surface. Before the SEM examination, the deposit surfaces were desiccated for 24 h and then coated with a thin layer of gold, approximately 10 nm thick, to facilitate SEM and profilometric studies. A non-contact optical profilometry method was used to assess the deposit's geometrical features. The measurements were conducted using a Taylor Hobson 3-D surface and film thickness optical profiler. Additionally, the TalySurf CCI, a commercial optical metrology software, was used to process the data. The distribution of pathogens within the deposits was also studied using the Andor Dragonfly confocal microscopy system. The bacteria were labelled with GFP, which has excitation and emission maxima at 375 nm and 509 nm, respectively. Fluorescence images were captured using a 10× objective, providing a field of view of $1450 \,\mu m \times 1450 \,\mu m$. Imaging was performed across multiple z-planes with a step size of 1 µm. The final composite image was obtained by superimposing images from several z-planes and stitching the superimposed images at various locations to reveal the overall bacterial distribution within the deposit. Live imaging, captured at a rate of one frame per second, revealed the movement of bacteria within the droplet during the drying process, both near the droplet edge and at the centre (refer to supplementary movies 4–7). The fluorescent tagged bacteria were tracked to generate the individual trajectory path lines using the TrackMate ImageJ plugin (Tinevez et al. 2017; Ershov et al. 2022) (refer to supplementary movies 8–9).

3. Results and discussions

3.1. Global overview

In this work, we study the mechanics of sessile blood drop evaporation (figure 2) using EDTA-based pure and bacteria-laden whole blood with varying levels of bacterial concentration theoretically and experimentally using lubrication theory, colour optical imaging and micro/nano-characterisation. The concentration ranges from those that are typically found in living organisms ($c \le 10^9$ CFU ml⁻¹) to exceedingly high concentration $(c \sim 10^{12} \text{ CFU ml}^{-1})$. Figure 2(a) depicts the schematic representation of an evaporating sessile droplet. Figure 2(b) represents the normalised volume regression of the evaporating droplet for various blood samples (pure and bacteria-laden). We observe that the volume regression is independent of the bacterial concentration range typically found in living organisms ($c \le 10^9$ CFU ml⁻¹). For exceedingly high bacterial concentration ($c \sim 10^{12}$ CFU ml⁻¹), the evaporation rate reduces slightly; however, the changes are not drastic. The normalised volume asymptotes the packed cell volume (PCV) of the blood sample at the end of evaporation. We further observe from figure 2(b) that the transient evaporation process can be subdivided into three stages (A, B and C) based on the evaporation rate. The first stage of evaporation (stage A) ends when the evaporation curves deviate from the initial linear evolution of a pure sessile evaporating droplet with an asymptotic form of normalised volume regression $V/V_0 \sim 1 - \gamma t$, where γ is the scale for the slope of the regression. The end of second stage (stage B) and the beginning of the final stage (stage C) occur when the normalised droplet volume approaches the packed cell volume asymptotically. Stage C represents the final and very slow evaporation rate where

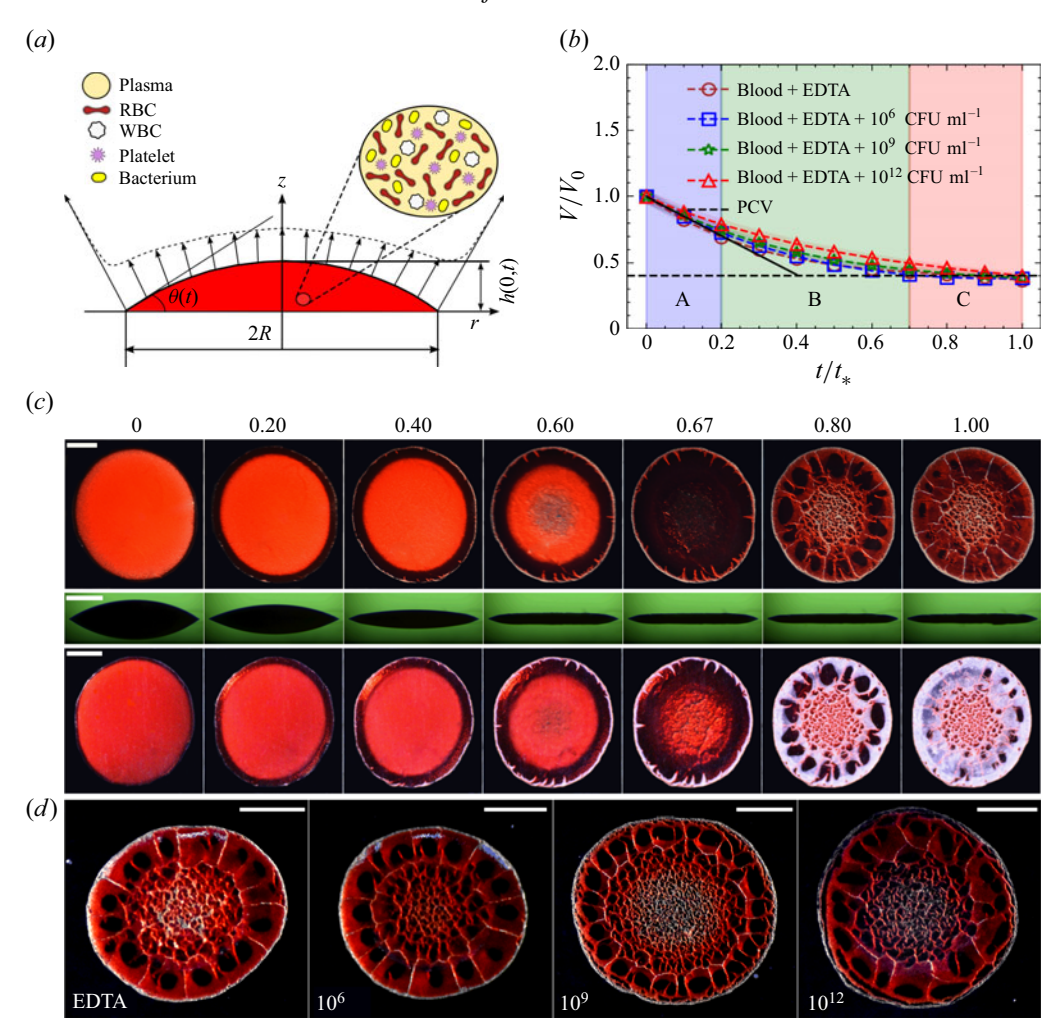


Figure 2. (a) Schematic of the coordinate system, composition of the blood and initial condition of sessile blood drop evaporation. (b) Non-dimensional volume (V/V_0) regression plotted as a function of non-dimensional time (t/t_*) for whole blood + EDTA, whole blood + EDTA + 10^6 CFU ml⁻¹ KP (*Klebsiella pneumoniae*) bacteria and whole blood + EDTA + 10^9 CFU ml⁻¹ KP bacteria. The different stages of sessile blood drop evaporation depicted as A, B and C. The solid black straight line denotes the linear evaporation regime from which the true regression curves deviate at the end of stage A. (c) Top view, side view and bottom view time sequence images of the evaporation process. Scale bar for the top, side and bottom view represents 1 mm. The time stamps are in non-dimensional units (t/t_*) . (d) Top view depicting the final precipitate at $t/t_* = 1$ for EDTA, 10^6 CFU ml⁻¹, 10^9 CFU ml⁻¹ and 10^{12} CFU ml⁻¹. The scale bar denotes 1 mm.

processes like major crack formation and precipitate delamination occur. Figure 2(c) represents the typical top, side and bottom view image sequences of the evaporation process (refer to supplementary movies 1, 2 and 3 to view the evaporation process through top, side and bottom imaging, respectively). Stage A (figure 2b,c; $t/t_* = 0-0.2$) is the fastest where edge evaporation dominates and leads to the formation of a gelated front propagating radially inwards. Here, t denotes the instantaneous time and t_* denotes the total evaporation time scale comprising all the three stages. The radially outward capillary flow generated by drop evaporation causes the RBCs to accumulate at the outer edge of the droplet. The intermediate stage B (figure 2b,c; $t/t_* = 0.2-0.7$) consists of gelation of the

entire droplet due to the radially inward propagating gelation front, and the simultaneous reduction of droplet height h(r, t) and contact angle $\theta(t)$ (refer to figure 2a for the various shape descriptors of a sessile droplet). The radially inward propagating gelation front leads to RBC deposition, causing the formation of a thick rim around the droplet periphery known as corona (Brutin et al. 2011). Gelation in stages A and B occurs due to the solgel phase transition. The sol-gel phase transition occurs when the solute concentration (RBCs here) becomes larger than a critical concentration. We unearth that the gelation of the entire droplet occurs in stage B. At the end of stage B, the gel formed contains some trace amounts of water. The trace amounts of water make the gel wet and stick (laminated) to the glass substrate due to the hydrophilic nature of the glass. Stage C (figure 2b,c; $t/t_* = 0.7 - 1.0$) is the final slowest stage of evaporation, where the wet gel formed during stage A and stage B transforms into a dry gel due to a very slow evaporation process. Due to the continued loss of water from the wet gel, the laminated regions adhered to the glass substrates undergo delamination. On further desiccation, the drying droplet results in high azimuthal stress, forming radial cracks in the corona region. Mudflat cracks are observed in the centre part of the evaporating droplet, where the drop thickness is relatively small and curvature is negligible. We further show that the drop evaporation rate and the corresponding dried residue pattern do not change appreciably within the parameter variation of the bacterial concentration typically found in living organisms (figure 2b). However, at exceedingly high concentration of 10¹² CFU ml⁻¹, the crack pattern in the peripheral corona region deviates from the patterns found at relatively lower concentration $(c \le 10^9 \text{ CFU ml}^{-1})$. Figure 2(d) shows the top view of the final precipitate at $t/t_* = 1$ for EDTA, 10^6 CFU ml^{-1} , 10^9 CFU ml^{-1} and $10^{12} \text{ CFU ml}^{-1}$. From figure 2(d), it is clearly evident that the cracks in the corona region of the dried precipitate deviates from the radial direction at very high bacterial concentration.

3.2. Coordinate system and sessile droplet evaporation physics

Figure 2(a) shows the schematic of the evaporating droplet and the associated coordinate system. An axisymmetric cylindrical coordinate system (r-z) is used to describe and analyse the evaporation process quantitatively. Here, r represents the radial coordinate and z represents the axial coordinate, the vertical axis along which the droplet liquid–vapour interface profile would be symmetric. In general, the sessile droplet can be described by certain geometrical shape descriptors like contact angle (θ) , contact radius (R) and drop central height (h(0, t)) for a particular initial droplet volume and substrate. For small Bond number $(Bo = \Delta \rho g l^2/\sigma < 1)$, the droplet geometry can be approximated by a spherical cap geometry (Hu & Larson 2002; Gennes *et al.* 2004; Clift, Grace & Weber 2005), where $\Delta \rho$ is the density difference at the liquid–air interface, g is the acceleration due to gravity, l is the characteristic length scale and σ is the liquid–air surface tension. For the current experiments, using $\Delta \rho \sim \mathcal{O}(10^3)$ kg m⁻³, $g \sim \mathcal{O}(10)$ m s⁻², $l \sim R \sim \mathcal{O}(10^{-3})$ m and $\sigma \sim \mathcal{O}(7 \times 10^{-2})$ N m⁻¹, we have $Bo \sim \mathcal{O}(10^{-1}) < 1$ and, hence, the spherical cap assumption can be used to describe the evaporating droplet. The interface profile of the sessile droplet is therefore given by (Hu & Larson 2002)

$$h(r,t) = \sqrt{\frac{R^2}{\sin^2 \theta} - r^2} - \frac{R}{\tan \theta}$$
 (3.1)

and the corresponding drop volume is given by

$$V(t) = \pi h(0, t) [3R^2 + h^2(0, t)]/6,$$
(3.2)

where $h(0, t) = R \tan(\theta(t)/2)$. In the case of blood drop evaporation, the spherical cap assumption would be valid up to a particular time scale $(t/t_* \sim 0.5)$ after which, deviation

from the spherical cap geometry becomes too large due to the effect of gelation. Initially (i.e. $t/t_* = 0$), the evaporative flux profile at the drop interface is highest at the drop contact line and least at the drop centre (refer to figure 2a). The diffusion-limited evaporation model can be used to approximate isothermal sessile drop evaporation for droplets in the size range of mm (i.e. $R \sim \mathcal{O}(10^{-3})$ m) to a very high degree of accuracy. The size where molecular reaction kinetics dominates diffusion evaporation phenomena occurs approximately at length scales of the order of 100 nm (Agharkar et al. 2024), which is considerably very small with respect to the typical length scale that we have in our current experiments, therefore, conforming to diffusion-limited drop evaporation. Drop evaporation, in general, can occur in various modes like CCR (constant contact radius) and CCA (constant contact angle) (Wilson & D'Ambrosio 2023) depending on the wettability of the substrate. For hydrophilic substrates with an initial acute contact angle, as is the present case, drop evaporation generally occurs in the CCR mode of evaporation. In the CCR mode of evaporation, the droplet's three-phase contact line is pinned throughout the evaporation process, while the contact angle decreases with time. For the present case of evaporating whole blood droplets, the evaporation occurs in CCR mode, as can be observed from the image snapshots in figure 2(c). The evaporation in CCR mode generates an capillary flow inside the droplet. For thin (i.e. small contact angles) droplets, the conservation of mass for the solvent in the evaporating droplet (water in general) is given by (Wilson & D'Ambrosio 2023)

$$\frac{\partial h}{\partial t} + \frac{1}{r} \frac{\partial (rh\langle u\rangle)}{\partial r} = -\frac{J}{\rho},\tag{3.3}$$

where $\langle u \rangle$ is the height average radial velocity, ρ is the liquid density and the evaporation flux J is given by

$$J = \frac{2Dc_v(1 - RH)}{\pi\sqrt{R^2 - r^2}} \tag{3.4}$$

for $0 \le r < R$, where D is the diffusivity of water vapour in air, c_v is the saturation concentration of water vapour at the droplet interface at a particular temperature and RH is the relative humidity. Using (3.4) in (3.3), the height averaged radial velocity can be computed as (Wilson & D'Ambrosio 2023)

$$\langle u \rangle = \frac{4Dc_v(1 - RH)}{\pi \rho \theta r} \left[1 - \left(1 - \frac{r^2}{R^2} \right)^{3/2} \right] \left(1 - \frac{r^2}{R^2} \right)^{-1/2},$$
 (3.5)

where $(r, \theta) \neq 0$. For particle-laden droplets, the radially outward capillary flow can cause edge deposition like the coffee ring effect (Deegan *et al.* 1997). For dilute concentration of particles and assuming negligible particle diffusion, the particle concentration c would satisfy (D'Ambrosio *et al.* 2023; Wilson & D'Ambrosio 2023)

$$\frac{\partial c}{\partial t} + \langle u \rangle \frac{\partial c}{\partial r} = \frac{Jc}{\rho h}.$$
(3.6)

The assumption of negligible particle diffusion could be understood from the Péclet number of the RBCs. The Péclet number in transport processes is the ratio of advective transport rate to diffusive transport. The major cellular component responsible for pattern formation is the aggregation and transport dynamics of the RBCs. Majorly, the RBCs are transported across the droplet through capillary-driven advection and diffusion of RBCs is negligible. The essential transport mode could be understood by analysing the scales of Péclet number for RBCs. The Péclet number for RBCs is defined as $Pe = uL/D_{RBCs}$,

where u is the characteristic velocity scale, L is the characteristic length scale of the flow and D_{RBCs} is the diffusivity of the RBCs in blood plasma. The scale of the diffusivity D_{RBCs} could be calculated using the Stokes-Einstein equation as $D_{RBCs} \sim$ $K_BT/6\pi \eta_P r_{RBCs}$ (Sadhal, Ayyaswamy & Chung 2012), where k_B is the Boltzmann constant, T is the absolute temperature in Kelvin, η_P is the plasma viscosity and r_{RBCs} is the characteristic length scale of an RBC. Using $k_B \sim 1.38 \times 10^{-23}$ J K⁻¹, $T \sim 300$ K, $\eta_P \sim 1.3 \times 10^{-3}$ Pa s and $r_{RBCs} \sim 4 \times 10^{-6}$ m, the diffusivity becomes $D_{RBCs} \sim 4.22 \times 10^{-14}$. Using $u \sim \mathcal{O}(10^{-6})$ m s⁻¹ and $L \sim \mathcal{O}(10^{-3})$ m, the corresponding Péclet number evaluates to $Pe \sim 2.37 \times 10^4$ indicating negligible effect of diffusion compared with advection. Diffusion can be important in a very thin region near the pinned contact line as was shown in recent works (Moore et al. 2021, 2022; Moore & Wray 2023). Moore et al. investigated the nascent coffee ring that forms when solute diffusion counters and balances advection. For very small capillary number and large Péclet number (as is the case for our current experiment), the importance of solute diffusion is confined to a very thin region (boundary layer) near the pinned contact line. Also, as can be observed through the nondimensional advection-diffusion equation, the Péclet number appears as a coefficient in the denominator of the diffusion term and can be neglected for very high Péclet number in general. Further, as diffusion is a physical process governed by random motion of particles, the particle size is an important parameter. Diffusion is important for small particle sizes typically of the order of $\sim \mathcal{O}(10-10^2)$ nm. In the current experiment, the typical length scale of the major particles (RBCs) are of the order of $\sim \mathcal{O}(10) \, \mu \text{m}$, which is at least 100times bigger than the particles for which diffusion becomes important. Therefore, we can safely neglect the diffusion of RBCs in the evaporating droplet.

Using (3.4), (3.5) and the method of characteristics for solving the first-order partial differential equation (PDE) for c, we have

$$c = c_0 \left[\left(\frac{\theta}{\theta_0} \right)^{-3/4} + \left(1 - \frac{r^2}{R^2} \right)^{3/2} - 1 \right]^{1/3} \left(1 - \frac{r^2}{R^2} \right)^{-1/2}, \tag{3.7}$$

where $c_0 = c_0(r)$ is the initial radial concentration field along the droplet radius. It is important to note that the concentration computed from (3.7) is only valid for thin droplets and dilute solution. The variation of evaporation flux, depth average radial velocity and depth average particle concentration as a function of radial coordinate is shown in figures S1-S3 of the supplementary material, respectively. It is important to note that the radial variation of evaporation flux, velocity and particle concentration from (3.4), (3.5) and (3.7) is a monotonically increasing function. Further from (3.5), (3.7), we can observe the singularity at the contact line r = R for both $\langle u \rangle$ and c. For thin drops and dilute concentration, the evaporative flux is independent of the height profile and the particle concentration, unlike blood drop evaporation where the dependence exists. For blood droplet evaporation, the solution for J, h and c cannot be obtained independently as depicted previously, and has to be obtained in a coupled manner (refer to § 3.4 for the details). This is due to the non-monotonic nature of the evaporation flux due to gelation. Further the non-trivial coupling between c, J and h also plays an important role as discussed in a later portion of the text (refer to $\S 3.4$). From figure 2(b), we can observe that the entire CCR mode of the evaporation process can be further subdivided into three stages, A, B and C, based on the descending rate of evaporation. Figure 2(b) represents the graph of normalised volume ratio (V/V_0) with normalised time (t/t_*) for the evaporating drop. Here, V denotes the instantaneous drop volume and V_0 denotes the initial drop volume. Here, t denotes the instantaneous time and t_* denotes the complete evaporation time scale (defined experimentally as the time instant where no significant changes are

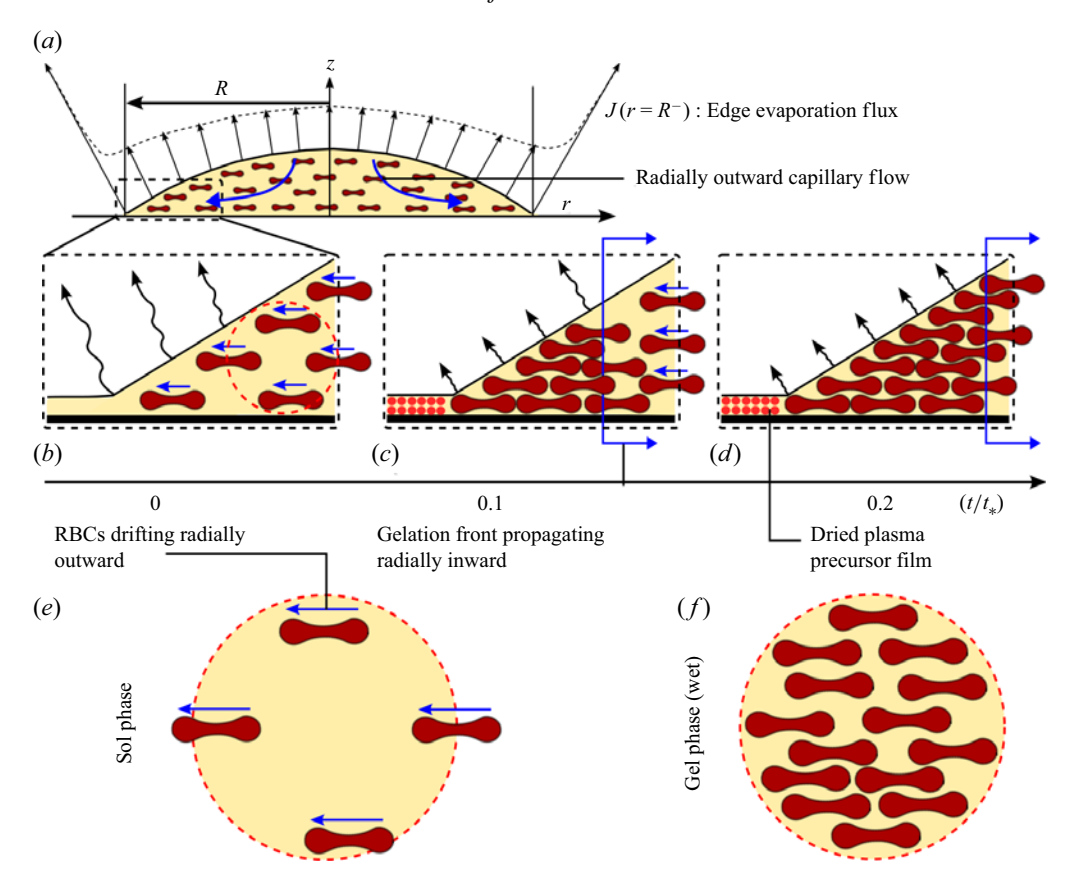


Figure 3. Schematic representation of the various processes occurring in stage A of blood droplet evaporation. (a) Initial configuration of the sessile blood droplet at $t/t^* = 0$ depicting the evaporative flux and the radial outward capillary flow inside the evaporating droplet. (b,c,d) Magnified view of the outer edge of the droplet depicting the precursor film and the outward transport of RBCs towards the edge at $(b) t/t^* = 0$, $(c) t/t^* = 0.1$ and $(d) t/t^* = 0.2$. The blue vertical line shows the gelation front propagating radially inwards. (e) A small control volume (CV) near the three-phase contact line depicting the sol phase in which RBCs are present inside the CV and getting transported across the surface of the CV. (f) Wet-gel phase in the CV as RBCs concentration increases.

observed in drop morphologies in all three views). The end of stage A (beginning of stage B) occurs when the regression curves deviate from the intial asymptotic linear evaporation regime of a pure sessile droplet. The initial linear regime is determined by curve fitting the initial regression data for all bacterial concentration and is shown as a black solid line in figure 2(b). The goodness of fit characterised by the coeffecient of determination is $R^2 = 0.95$. Stage B ends (stage C begins) when V/V_0 approaches the packed cell volume (PCV). From figure 2(b,c), we can observe that stage A corresponds to $t/t_* = 0.00$, stage B corresponds to $t/t_* = 0.00$, and stage C corresponds to $t/t_* = 0.00$. The mechanics of the individual stages during drop evaporation are discussed now.

3.3. Stages of blood drop evaporation

3.3.1. *Stage A*

Figure 3 shows the schematic representation of various processes that occur during stage A. Figures 2(a) and 3(a) show the initial configuration of the evaporating blood droplet. The sample blood droplet is a suspension of cellular elements like RBCs, WBCs,

D. Roy and others

platelets and bacteria (for bacteria-laden drops) suspended in plasma. However, due to the very high number density of RBCs, blood can be approximated as a binary suspension to first approximation. Blood droplet evaporation on hydrophilic substrates occurs in CCR mode with a constant contact radius R due to the pinning of the contact line (refer to side view panel of figures 2(c), 4(a), 5(a), 6(b) and 7(a) and video data (supplementary movie 2)). For small drops, the droplet shape at the initial time can be approximated by a spherical cap. The evaporation flux along the droplet interface monotonically increases with radial coordinate r and peaks at the contact line at $t/t_* = 0$. The non-uniform evaporation flux along the drop interface generates a radially outward capillary flow that causes the RBCs to be transported towards the contact line (refer to supplementary movies 1, 4, 5, 6, 7, 8, 9). Figure 3(b,c,d) shows the magnified view near the contact line at $t/t_* = 0, 0.1, 0.2,$ respectively. At the initial time of drop evaporation, a very thin precursor film of plasma exists at the outer edge of the droplet, which slowly solidifies (depicted schematically as red filled circles in figures 3c and 3d) (refer to supplementary movies 1 and 3 for top and bottom view video data, respectively). The precursor film is devoid of RBCs as the dimension of the precursor film is smaller than a single RBC length scale. The outer radial capillary flow (shown by the blue arrow) (refer to supplementary movies 6, 7) causes the RBCs to accumulate, forming a gel phase. In supplementary movies 6 and 7, the dark regions which move radially outwards are the RBCs, and the green illuminated objects are the bacteria and their colonies which also move radially outwards through the gaps in between the RBCs due to the mean capillary flow inside the evaporating droplet. After the initial gelation of the three-phase contact line, a gelation front radially propagating inward is observed (vertical blue line in figure 3c,d) (refer to supplementary movies 1, 3). Further, the concentration of RBCs increases at the outer periphery, reducing evaporation flux at the drop interface near the contact line. A small dotted circle representing a control volume (CV) near the contact line is shown in figure 3(b). Figure 3(e) shows the zoomedin view of the CV. The blood suspension inside the CV is initially in the sol phase. However, due to the outward capillary flow, the concentration of RBCs inside the control volume increases, leading to a phase transition that forms a wet-gel phase (figure 3f). The evaporative flux over the wet-gel region reduces significantly, as depicted in the schematic by the reduction of the length of the squigly black arrows (figure 3b-d) depicting the evaporative flux. Sol-gel transition initiates at the three-phase contact line as the concentration approaches a critical gelation concentration c_g (refer to § 3.4 for a detailed discussion).

Figure 4(a) shows the top, side and bottom image sequence for stage A of the evaporating blood droplet in the top, middle and bottom panels, respectively. The constant contact pinned radius is denoted by R and the gelation radius by r_g (refer to the yellow circles in the top view image panel of figure 4a). The drop contact angle is represented by θ and the drop centre height by h = h(0, t). Figure 4(b,c) shows the schematic representation of the evaporation stage A at $t/t_* = 0$ and $t/t_* = 0.2$, respectively. Note the increase in concentration of RBCs and the corresponding reduction of evaporation flux depicted schematically in figure 4(c). Figure 4(d) shows the evolution of various normalised geometrical parameters G(t) like normalised contact angle (θ/θ_0) and normalised contact radius (R/R_0) confirming CCR mode of drop evaporation. Figure 4(e) also shows the evolution of other normalised geometrical parameters like normalised droplet centre height (h/h_0) and normalised gelation radius (r_g/r_{g0}) during stage A. It can be observed that the droplet height reduction is faster than that of the gelation front propagation. The faster reduction of central height is one of the important causes of the distinct dried droplet residue profile formed in stage C, which will be discussed later in the text.

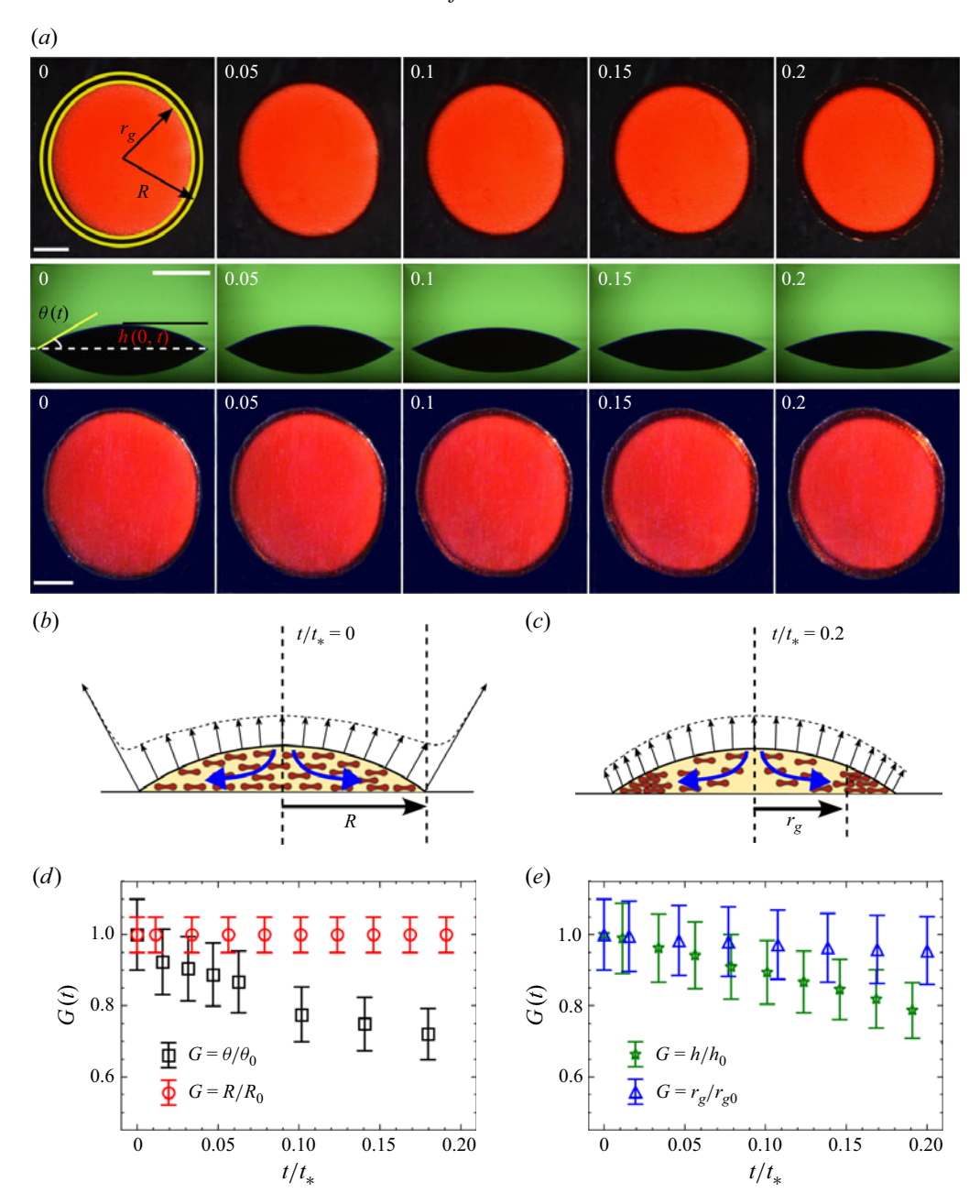


Figure 4. (a) Top, side and bottom view time sequence images of stage A at different non-dimensional time instants $t/t_* = 0$, 0.05, 0.1, 0.15, 0.2. Scale bar for top, side and bottom view represents 1.2, 1.3 and 1 mm, respectively. (b) Schematic representing the initial configuration of the evaporating droplet $(t/t_* = 0)$. (c) Schematic representing the evaporating droplet at the end of evaporation stage A $(t/t_* = 0.2)$ (d,e) Non-dimensional geometrical drop parameters G(t) (normalised contact angle (θ/θ_0) , normalised contact radius (R/R_0) , normalised drop height (h/h_0) and normalised gelation radius (r_g/r_{g0})) evolution as a function of non-dimensional time t/t_* .

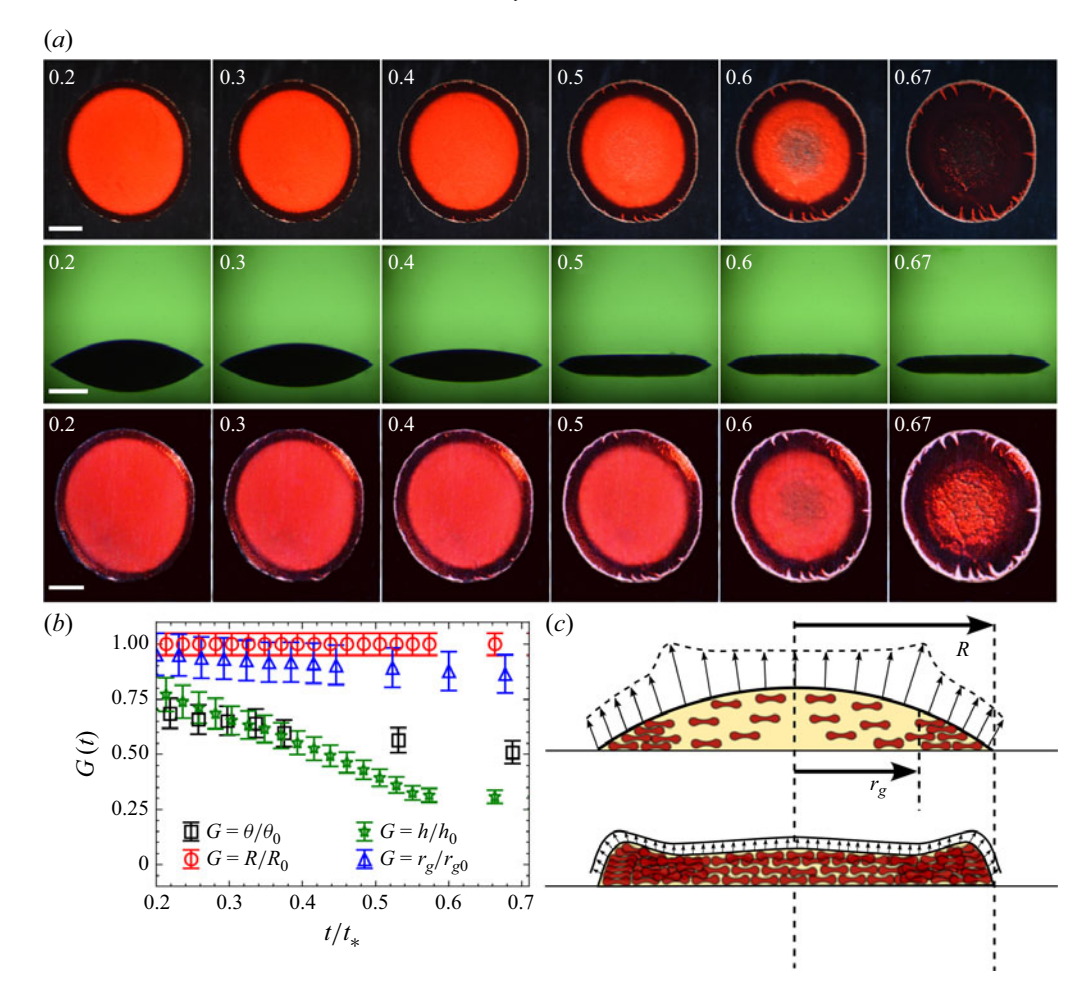


Figure 5. (a) Top, side and bottom view time sequence images of stage B at various non-dimensional time instants $t/t_* = 0.2$, 0.3, 0.4, 0.5, 0.6, 0.67. The scale bar represents 1 mm. (b) Non-dimensional geometrical drop parameters G(t) (normalised contact angle (θ/θ_0) , normalised drop height (h/h_0) , normalised contact radius (R/R_0) and normalised gelation radius r_g/r_{g0}) evolution as a function of non-dimensional time t/t_* . (c) Schematic representing the evaporating droplet at the beginning of stage B $(t/t_* = 0.2)$ and end of stage B $(t/t_* \sim 0.67 - 0.7)$.

3.3.2. *Stage B*

Stage B of the evaporation process spans from $t/t_* = 0.2$ to 0.7 and has the longest duration. In this stage, the gelation front propagates further radially inwards. As the droplet evaporates in CCR mode, the contact line is pinned, but the droplet contact angle and its corresponding maximum height decreases monotonically. As the droplet evaporates, the outward capillary flow causes a depletion of RBCs in the centre, allowing the droplet interface to change its curvature smoothly. Figure 5(a) shows the top, side and bottom view image sequence during stage B of evaporation. The time stamps are normalised time (t/t_*) . Figure 5(b) shows the droplet non-dimensional geometrical parameters G(t) evolution as a function of normalised time. Various parameters like normalised contact angle (θ/θ_0) , normalised height h/h_0 , normalised contact radius (R/R_0) and normalised gelation radius (r_g/r_{g0}) is plotted in black, green, red and blue, respectively. It is important to note that at approximately $(t/t_* = 0.5 - 0.6)$, there is a significant reduction of the

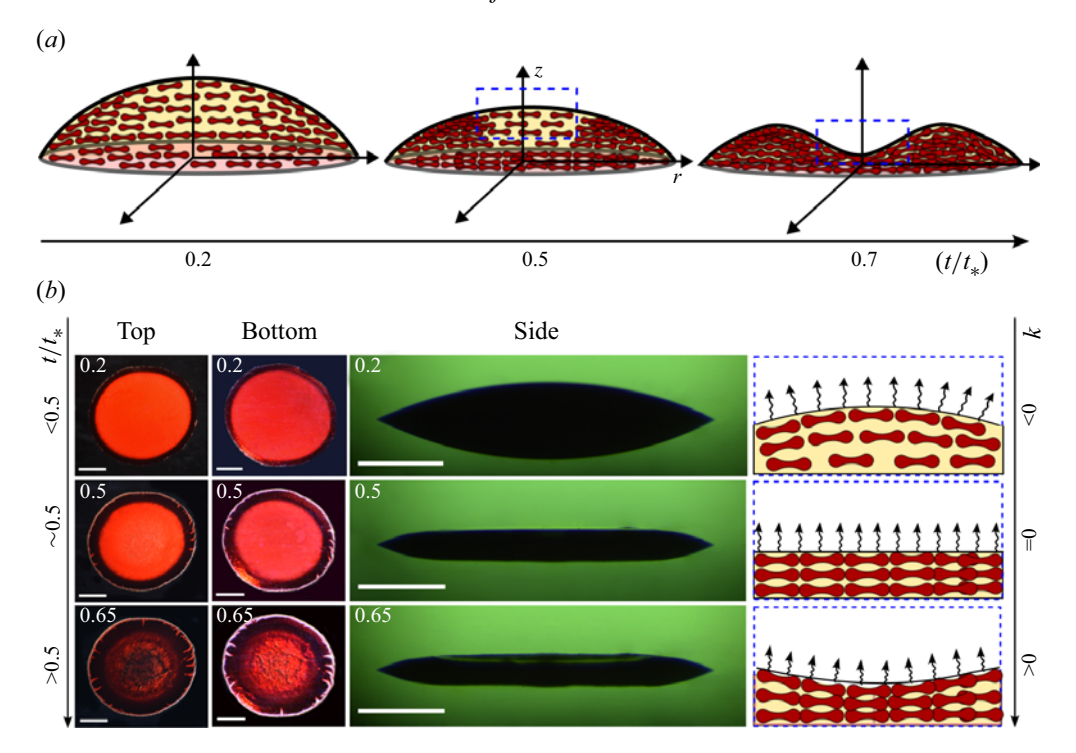


Figure 6. (a) Three-dimensional schematic representation of blood droplet evaporation in stage B from $t/t_* = 0.2$ to 0.7. (b) Top, bottom, side and schematic image sequence depicting curvature evolution and precipitate formation at $t/t_* < 0.5$, ~ 0.5 , >0.5. The scale bar represents 1 mm.

droplet height compared with its contact angle signifying the deviation of the droplet shape from spherical cap approximation. Figure 5(c) shows a schematic representation of the starting $(t/t_*=0.2)$ and ending state $(t/t_*\sim0.67-0.7)$ of stage B. Here, R denotes the contact radius and r_g denotes the gelation front radius. Notably, the distinct colour change in the top view at the end of stage B $(t/t_*=0.67)$ signifies the completion of the gelation of the entire droplet. At the end of stage B, the entire droplet undergoes a solgel phase transition to a final wet-gel form. The wet-gel phase contains very small (trace) amounts of liquid water that evaporates in the next stage, C. We can also observe from the side view image panel that there is negligible change in droplet geometry, signifying the completion of gelation for the entire droplet.

Figure 6 shows a schematic representation of the various processes occurring during stage B of evaporation. Figure 6(a) shows a 3-D schematic of the vertical cross-section of the droplet interface curvature change as evaporation proceeds through stage B at $t/t_* = 0.3, 0.5, 0.7$. Figure 6(b) shows the top, bottom, side and the schematic representation of the droplet interface undergoing monotonic curvature (k) change from k < 0 to k = 0, to k > 0 at $t/t_* < 0.5, t/t_* \sim 0.5-0.6$ and $t/t_* > 0.6$.

3.3.3. *Stage C*

Figure 7(a) shows the image sequence of the top, side and bottom view of the desiccating drop. Notice the distinct colour change in the top and bottom views as the drop transforms from wet gel to dry gel. The colour change is the signature for the loss of water (and corresponding delamination from the substrate) from the wet-gel precipitate and transforming it into a dry-gel form. From both the top and bottom views, we can observe

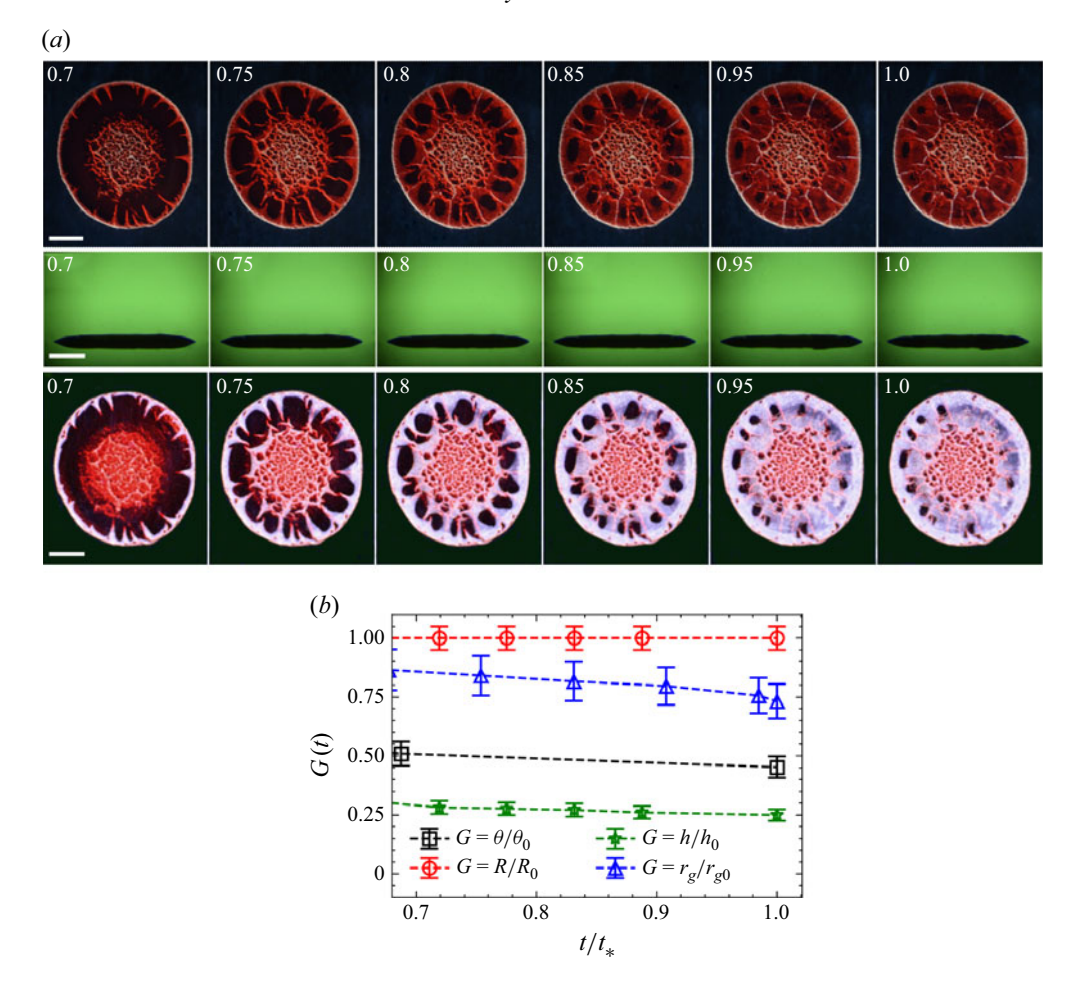


Figure 7. (a) Top, side and bottom view time sequence images of stage C at non-dimensional time instants $t/t_* = 0.7, 0.75, 0.8, 0.85, 0.95, 1.0$. The scale bar represents 1 mm. (b) Non-dimensional geometrical drop parameters G(t) (normalised contact angle (θ/θ_0) , normalised drop height (h/h_0) , normalised contact radius (R/R_0) and normalised gelation radius r_g/r_{g0}) evolution as a function of non-dimensional time t/t_* .

the evaporation process of the trace amounts of water present at the beginning of stage C. Dessication stresses are developed as the drop undergoes further evaporation, forming various types of cracks. Radial cracks are observed in the thicker outer rim region, whereas mudflat cracks are observed in the centre and the contact line region. Figure 7(b) shows the slow variation of the non-dimensional geometric parameters such as contact angle, drop centre height, contact radius and gelation radius as a function of non-dimensional time. It is important to contrast the slow variation of the geometrical parameters in stage C from the relatively fast variation in stages A and B. The role of bacteria on blood droplet evaporation and final precipitate can be understood by comparing the time series images of the evaporating droplet. Figure 8(a) shows the image snapshots for 0, 10^6 , 10^9 and 10^{12} CFU ml⁻¹ bacterial concentration at non-dimensional time $t/t_* = 0$, 0.20, 0.40, 0.60, 0.67, 0.80, 1.00. Figures 8(b), 8(c) and 8(d) depict the time evolution of normalised contact radius R/R_0 , normalised central height h(0, t)/h(0, 0) and normalised contact angle θ/θ_0 , respectively, for the evaporating droplet of 0, 10^6 , 10^9 and 10^{12} CFU ml⁻¹ bacterial concentration. From figure 8(b), it is evident that the

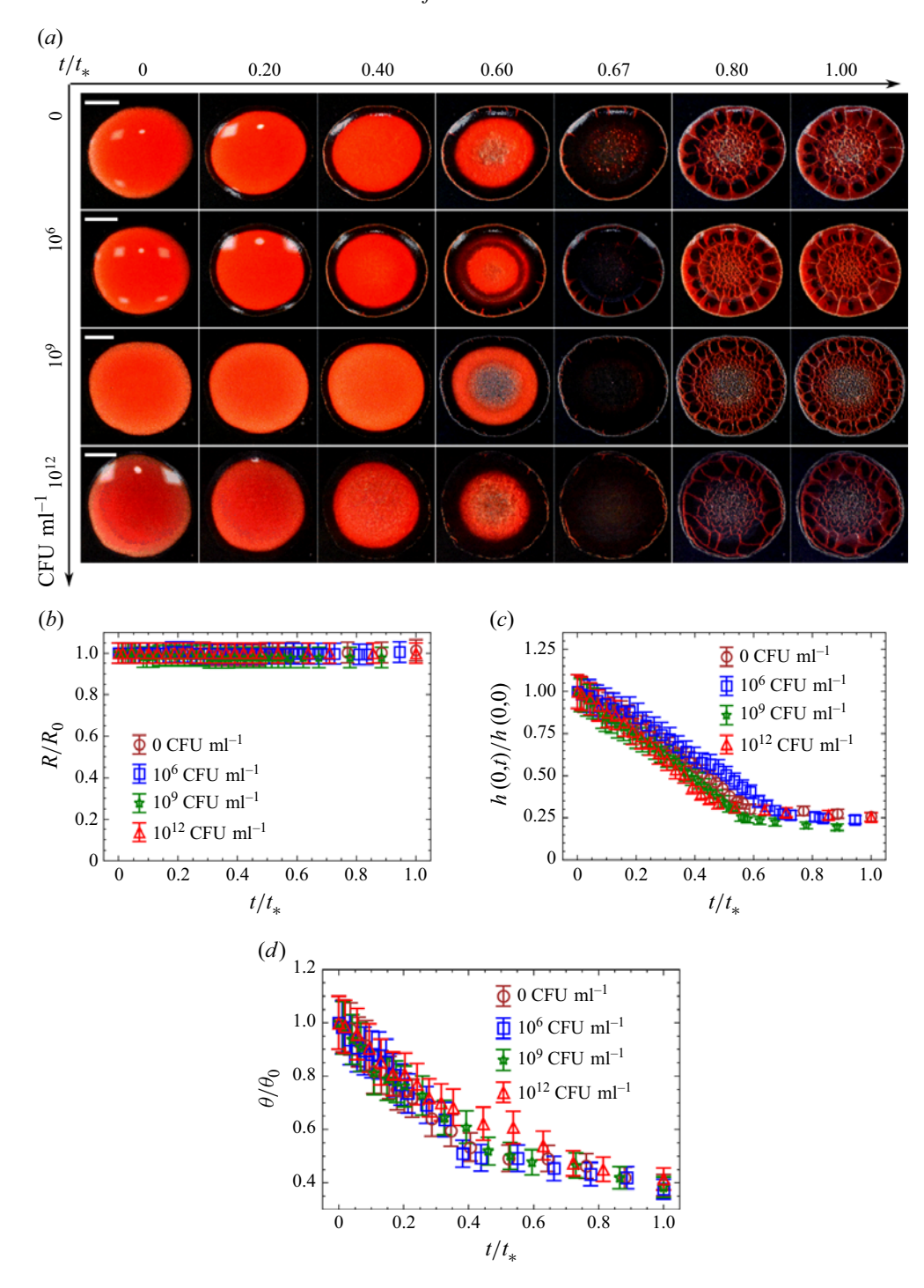


Figure 8. (a) Comparative time series depicting top view of evaporating blood droplet for 0, 10^6 , 10^9 and 10^{12} CFU ml⁻¹ for $t/t_* = 0$, 0.20, 0.40, 0.60, 0.67, 0.80, 1.00. (b) Normalised droplet contact radius as a function of normalised time for 0, 10^6 , 10^9 and 10^{12} CFU ml⁻¹ bacterial concentration. (c) Normalised droplet central height as a function of normalised time for 0, 10^6 , 10^9 and 10^{12} CFU ml⁻¹ bacterial concentration. (d) Normalised droplet contact angle as a function of normalised time for 0, 10^6 , 10^9 and 10^{12} CFU ml⁻¹ bacterial concentration.

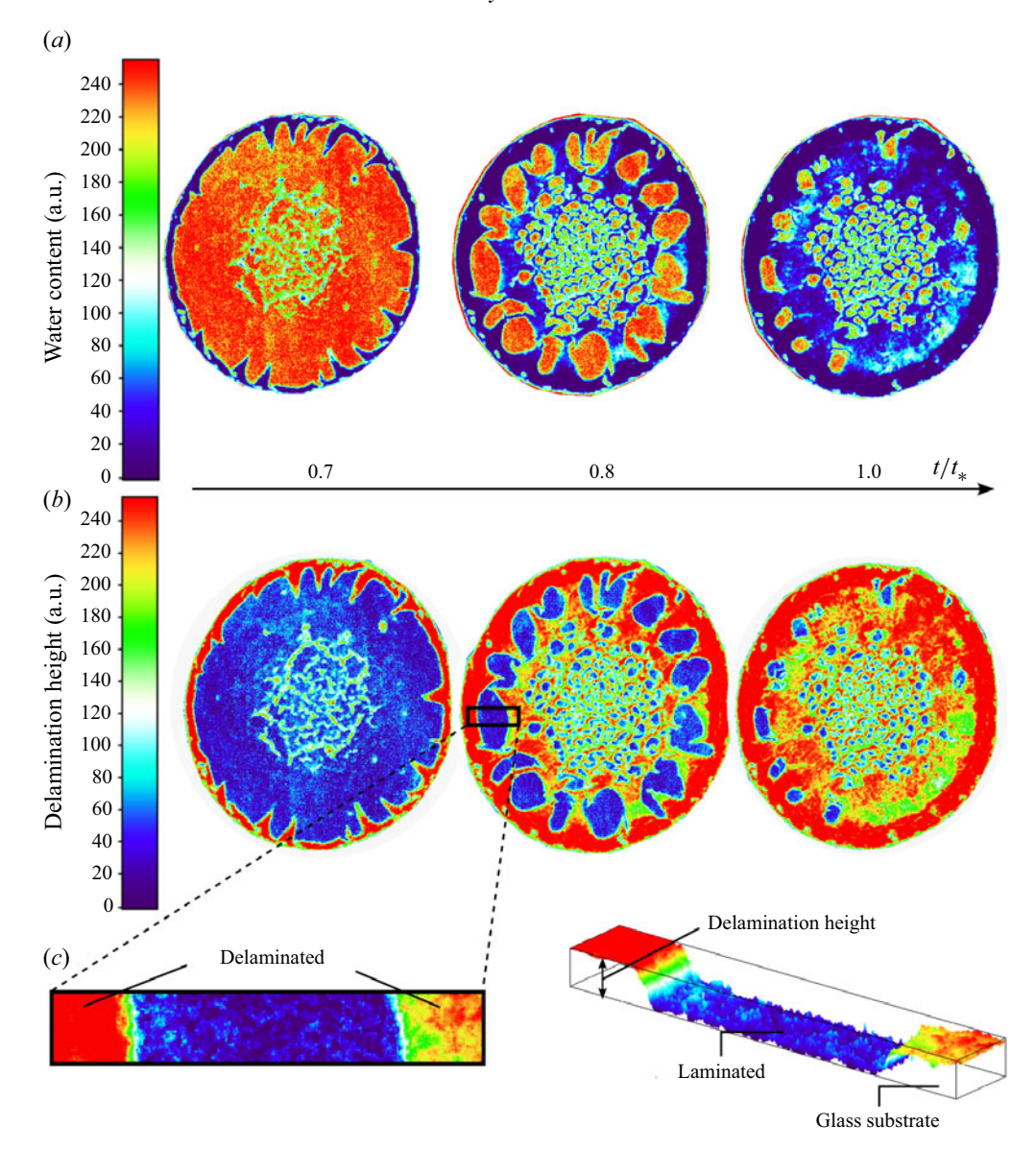


Figure 9. (a) Evolution of entrapped water evaporation as a function of non-dimensional time in stage C represented as an intensity colour map. (b) Evolution of the two-dimensional (2-D) delamination height as a function of non-dimensional time in stage C represented as an intensity colour map. (c) Magnified view depicting a typical laminated and delaminated region at the corona of dried blood residue at $t/t_* = 0.8$.

entire evaporation of the droplet occurs in pinned mode. Using figures 8(b), 8(c), 8(d) and 2(b), it is evident that evaporation is independent of bacterial concentration up to 10^9 CFU ml⁻¹. The volume regression curve for 10^{12} CFU ml⁻¹ (figure 2b) shows very small decrease in evaporation rate compared with a lower concentration up to 10^9 CFU ml⁻¹; however, the changes are very small. Although the evaporation characteristics do not change drastically for 10^{12} CFU ml⁻¹ in comparison to 10^9 CFU ml⁻¹, the final crack precipitate pattern of 10^{12} CFU ml⁻¹ changes from that of a lower bacterial concentration of 10^9 CFU ml⁻¹ (refer to § 3.5 and figure 13). Figure 9(a) shows the evaporation of the

entrapped water in the wet-gel phase as a function of non-dimensional time represented as an intensity colour map in arbitrary units (a.u.) for effective visualisation. Figure 9(b) denotes the time sequence of 2-D delamination height represented as an intensity colour map in arbitrary units (a.u.) during wet gel to dry gel transformation in stage C. Figure 9(c) depicts a magnified view of the corona region of the dried blood precipitate highlighting regions like laminated and delaminated sections over the glass substrate. The dried residue undergoes a lamination-to-delamination transition as the wet gel transforms into a dry gel. The trace amounts of water present in the wet-gel phase (red region in the intensity colour map shown in figure 9a) cause the wet gel to adhere to the glass substrate (blue region in the intensity colour map shown in figures 9b and 9c) due to the hydrophilic nature of the glass substrate. However, on further desiccation, the water content in the laminated region decreases and leads to delamination from the substrate due to the phobic nature of the residual glycoproteins found on the surface of the RBCs (Brutin *et al.* 2011). The primary functionality of the glycoproteins is to minimise wettability from a surface.

3.4. Generalised mechanics of blood drop evaporation

The initial capillary flow initiated due to the non-uniform evaporation flux over the drop surface can be modelled using Stokes flow in cylindrical coordinates (refer to figures 2a and 3a). We follow the analysis of Brutin *et al.* (2011), Tarasevich *et al.* (2011) and Sobac & Brutin (2011) very closely for computing the dynamics of drop evaporation. From the radial component of the Stokes equation along with the thin film approximation (lubrication approximation), we have

$$\frac{\partial p}{\partial r} = \eta \frac{\partial^2 u}{\partial z^2}. (3.8)$$

In (3.8), the momentum diffusion is assumed to be negligible in the flow radial direction r in comparison to the vertical z direction due to the aspect ratio of the geometry (thin film approximation). In our experiments, we are dealing with droplets whose width is at least one order larger than the central height of the droplet and have relatively small contact angles due to hydrophilic substrates. Hence, it is evident from mass conservation that radial velocity will be significantly higher than the vertical component of velocity. The velocity profile in the vertical direction is due to the effect of momentum diffusivity; however, the variation in droplet velocity in the radial direction is majorly driven by the droplet shape (spherical cap). Hence, the effect of radial momentum diffusion will become important for droplets with aspect ratio close to unity and have relatively higher contact angles (hydrophobic substrates), which is unlike the current scenario which justifies the negligible effect of radial momentum diffusion. Therefore, from the axial component of the Stokes equation, we have

$$\frac{\partial p}{\partial z} = 0, (3.9)$$

where p is the pressure, r is the radial coordinate, η is the drop viscosity, u is the radial velocity and z is the axial coordinate. Assuming cylindrical symmetry about the vertical axis, the continuity equation can be written as

$$\frac{1}{r}\frac{\partial(ru)}{\partial r} + \frac{\partial w}{\partial z} = 0. \tag{3.10}$$

The boundary condition for pressure field on the drop surface z = h(r, t) is given by

$$p|_{z=h(r,t)} = -\sigma k, (3.11)$$

where σ is the surface tension and k is the curvature of the drop interface given by

$$k = \frac{1}{r} \frac{\partial}{\partial r} \left(r \frac{\partial h}{\partial r} \right). \tag{3.12}$$

Further, at the drop interface z = h(r, t), we have

$$\left. \frac{\partial u}{\partial z} \right|_{z=h(r,t)} = 0 \tag{3.13}$$

owing to the fact that the radial velocity u has negligible variation in the axial direction z. The no slip and no penetration boundary condition at the surface of the substrate z=0 ensures

$$u|_{z=0} = 0 (3.14)$$

and

$$w|_{z=0} = 0. (3.15)$$

Using (3.10)–(3.15), the radial velocity u can be written as

$$u = -\frac{\sigma}{\eta} \frac{\partial}{\partial r} \left(\frac{1}{r} \frac{\partial}{\partial r} \left(r \frac{\partial h}{\partial r} \right) \right) \left(\frac{z^2}{2} - hz \right). \tag{3.16}$$

The z component of fluid velocity is given by

$$w = \frac{\sigma}{r} \frac{\partial}{\partial r} \left(\frac{r}{\eta} \frac{\partial}{\partial r} \left(\frac{1}{r} \frac{\partial}{\partial r} \left(r \frac{\partial h}{\partial r} \right) \right) \left(\frac{z^3}{6} - h \frac{z^2}{2} \right) \right). \tag{3.17}$$

Integrating (3.16) with respect to z, the droplet height average radial velocity $\langle u \rangle$ is given as

$$\langle u \rangle = \frac{1}{h} \int_{0}^{h} u dz = \frac{h^{2} \sigma}{3 n} \frac{\partial}{\partial r} \left(\frac{1}{r} \frac{\partial}{\partial r} \left(r \frac{\partial h}{\partial r} \right) \right).$$
 (3.18)

Using the continuity equation for the conservation of mass of the volatile component (here, solvent majorly is the water content of the blood drop), the average radial velocity from (3.18), the dynamical equation for the drop height is given as

$$\frac{\partial h}{\partial t} = -\frac{1}{r} \frac{\partial (rh\langle u \rangle)}{\partial r} - \frac{J}{\rho},\tag{3.19}$$

where J is the evaporation flux and ρ is the density of the droplet. Similarly, using the continuity equation for the non-volatile component, i.e. solute (conservation of mass for the solute; here, the major fraction is the RBCs), the dynamics of the solute concentration c is given as

$$\frac{\partial(hc)}{\partial t} = -\frac{1}{r}\frac{\partial}{\partial r}(rhc\langle u\rangle). \tag{3.20}$$

For small drop size where gravity is negligible compared with surface tension effects, the drop shape can be approximated by a spherical cap model. However, the spherical cap model leads to singularities in the flow velocity and solute concentration (RBCs here) near the contact line. As a result, we replace the initial drop shape by a paraboloid of revolution without the loss of generality as a initial condition. The initial drop shape is therefore given by

$$h|_{t=0} = h_f + h_0 \left(1 - \left(\frac{r}{R}\right)^2\right),$$
 (3.21)

where h_f is the drop height at the edge that corresponds to the precursor plasma film,

$$h|_{r=R} = h_f.$$
 (3.22)

The sum of h_f and h_0 represents the central drop height thickness, i.e. at r = 0. Owing to the constant contact radius (CCR) mode of drop evaporation, the contact line of the drop is pinned and hence the radial velocity vanishes. The radial velocity also goes to zero at r = 0 due to vanishing curvature at the centre. Therefore, the boundary condition for the height average radial velocity $\langle u \rangle$ to solve (3.19) and (3.20) simultaneously is given by

$$\langle u \rangle|_{r=0} = \langle u \rangle|_{r=R} = 0. \tag{3.23}$$

The symmetry condition for the drop height profile gives

$$\left. \frac{\partial h}{\partial r} \right|_{r=0} = 0. \tag{3.24}$$

Similarly, the symmetry condition for solute concentration is given by

$$\left. \frac{\partial c}{\partial r} \right|_{r=0} = 0. \tag{3.25}$$

The initial solute concentration field is given by a known function f(r) of the radial coordinate

$$c(r, 0) = f(r).$$
 (3.26)

We solve the equations for the drop height, solute concentration and evaporation flux in non-dimensional coordinate space. The drop height is normalised with respect to initial drop height h_0 as $h_f \ll h_0$, i.e. $\bar{h} = h/h_0$. The radial coordinate r is normalised with respect to drop contact radius R, i.e. $\bar{r} = r/R$. The height average radial velocity $\langle u \rangle$ is normalised with respect to the viscous velocity scale $u_c = \eta_0/\rho h_0$, i.e. $\bar{u} = \langle u \rangle/u_c$. Here, η_0 is the viscosity of the solvent. The time scale t is normalised by a reference time scale R/u_c , i.e. $\bar{t} = tu_c/R$. The vapour flux t is normalised by a reference flux t is the difference between substrate and the saturation temperature, and t is the latent heat of vapourisation. The solute concentration t0 was normalised by the gelation concentration t1 t2. Using the above-mentioned normalised variables, (3.19) and (3.20) can be non-dimensionalised and written as a vector equation with t3 and t4 t5 expressed as a column vector

$$\frac{\partial \bar{F}}{\partial \bar{t}} + \bar{u} \frac{\partial \bar{F}}{\partial \bar{r}} = \bar{f},\tag{3.27}$$

where the column vectors \bar{F} and \bar{f} are given by

$$\bar{F} = \begin{bmatrix} \bar{h} \\ \bar{c} \end{bmatrix} \tag{3.28}$$

and

$$\bar{f} = \begin{bmatrix} -\frac{\bar{h}}{\bar{r}} \frac{\partial}{\partial \bar{r}} (\bar{r}\bar{u}) - E\bar{J} \\ \frac{E\bar{c}\bar{J}}{\bar{h}} \end{bmatrix}, \tag{3.29}$$

where

$$\bar{u} = \frac{\bar{h}^2}{3Ca} \frac{\partial}{\partial \bar{r}} \left(\frac{1}{\bar{r}} \frac{\partial}{\partial \bar{r}} \left(\bar{r} \frac{\partial \bar{h}}{\partial \bar{r}} \right) \right). \tag{3.30}$$

Here, $E = k_T \Delta T / \epsilon \eta_0 L$ and $Ca = \eta u_c / \epsilon^3 \sigma$ represent the evaporation and capillary number, respectively, where $\epsilon = h_0 / R$. The blood viscosity η dependence on the RBCs haematocrit Ht is given as (Lee Waite et al. 2007; Bergel 2012)

$$\eta = \eta_0 \left(\frac{1}{1 - \alpha Ht} \right), \tag{3.31}$$

where

$$\alpha = 0.076e^{2.49Ht + (1107/T)e^{-1.69Ht}}$$
(3.32)

and T is the temperature in Kelvin. The ratio of η/η_0 as a function of Ht is given in figure S4 of the supplementary material. From supplementary figure S4, it is evident that η increases monotonically with Ht. Here, Ht physically represents the volume fraction of RBCs in the blood droplet. The blood viscosity measured for the blood samples as a function of bacterial concentration are of the order of $2-4 \times 10^{-1}$ Pa s at a shear rate of 0.1 s⁻¹, which corresponds to a very high viscosity value (refer to the viscosity strain curve obtained from viscosity experiments in supplementary figure S5). Therefore, as the blood drop evaporates, Ht further increases causing an equivalent increase in blood viscosity and capillary number Ca, which further reduces the flow velocity scale \bar{u} inside the evaporating droplet, as $\bar{u} \propto Ca^{-1}$. The droplet precipitate thickness therefore becomes very weakly coupled to the flow velocity. The evaporative mass flux is modelled using techniques from heat transfer analysis (Anderson & Davis 1995) and also assuming that the vapour density vanishes at the sol-gel propagating front; i.e. the evaporative flux goes to zero as the concentration reaches a critical value of $\bar{c} = 1$ ($c = C_g$) during solgel phase transition at the propagating front. The dimensionless evaporation flux hence can be modelled as (Fischer 2002; Jung et al. 2009; Bhardwaj, Fang & Attinger 2009; Okuzono et al. 2010)

$$\bar{J}(\bar{r},\bar{t}) = \frac{1-\bar{c}^2}{k_d + \bar{h}},$$
 (3.33)

where k_d is a dimensionless non-equilibrium parameter. The range of k_d is such that $k_d \rightarrow \infty$ for non-volatile liquids and $k_d \rightarrow 0$ for volatile liquids. The form of (3.33) is based on the observation that higher concentration of RBCs will reduce the evaporation flux and the flux goes to zero at some critical concentration ($\bar{c}=1$) corresponding to a sol-gel phase transition. The squared (quadratic) concentration term is typically not obvious and depends on the requirement of no change in evaporative flux with respect to a concentration change up to a first-order change about $\bar{c}=0$. The quadratic term is the lowest order term to satisfy the criterion $(\partial \bar{J}/\partial \bar{c})|_{\bar{c}=0}=0$. The initial condition for the non-dimensional concentration profile required to solve (3.27) is given by

$$\bar{c}(r,0) = 2 - \bar{c}_0 + \frac{2(\bar{c}_0 - 1)}{1 + e^{w(\bar{r} - 1)}},$$
(3.34)

where w is a measure of a characteristic length over which the concentration of colloidal particles increases rapidly. From the above-mentioned distribution, it is important to note that $\bar{c}(0,0) \simeq 0$ and $\bar{c}(1,0) = 1$, suggesting the initial concentration at the edge of the droplet is equal to the gelation concentration (gelation has already occurred at the outer edge of the droplet contact line). Using $D \sim 2.61 \times 10^{-5}$ m² s⁻¹, $c_v \sim 2.32 \times 10^{-2}$ kg m⁻³, $k \sim \mathcal{O}(1)$ W mK⁻¹, $\Delta T \sim 75$ K, $\eta_0 \sim 5 \times 10^{-3}$ Pa s, $L \sim 2.25 \times 10^6$ J kg⁻¹, $\epsilon \sim 0.4$, the system of differential equations for \bar{h} and \bar{c} given by (3.27) is computed using finite difference methods for $E \sim 10^{-2}$ and $Ca \sim 6 \times 10^{-5}$ corresponding to whole

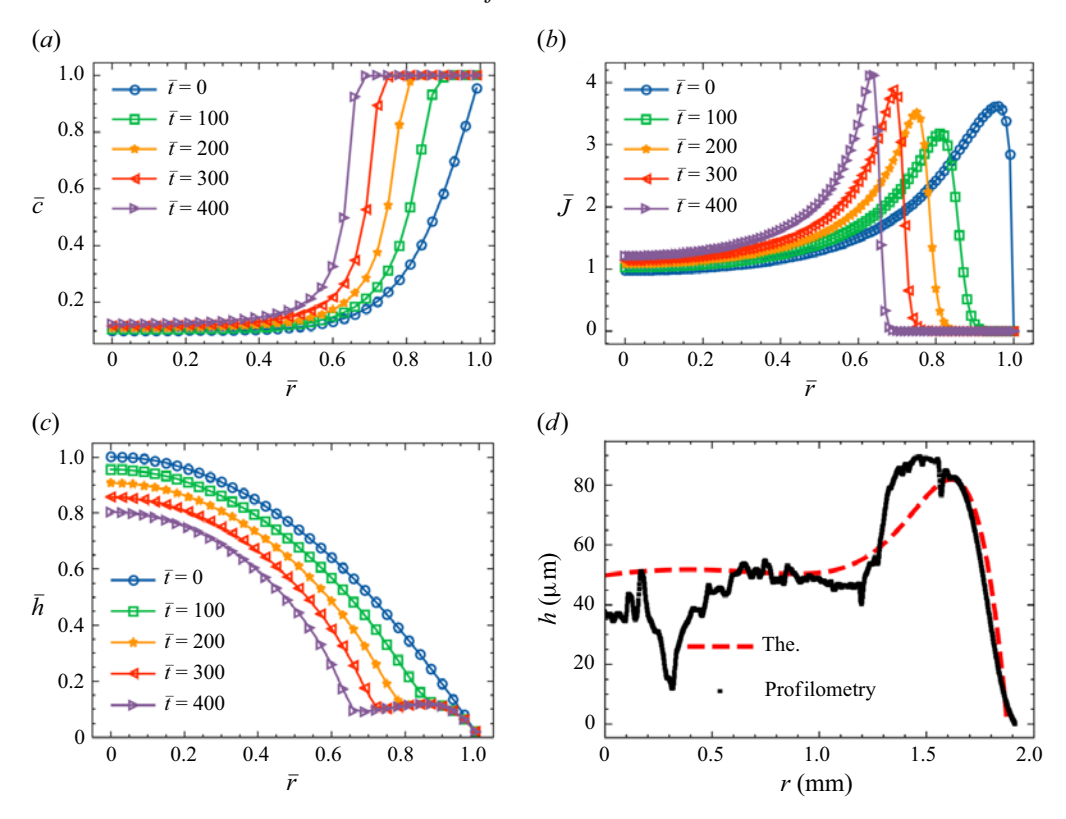


Figure 10. (a) Non-dimensional concentration field plotted as a function of non-dimensional radial coordinate at various non-dimensional time instants $\bar{t} = 0$, 100, 200, 300, 400. (b) Non-dimensional evaporation flux plotted as a function of non-dimensional radial coordinate at various non-dimensional time instants $\bar{t} = 0$, 100, 200, 300, 400. (c) Non-dimensional drop height variation as a function of non-dimensional radial coordinate at various non-dimensional time instants $\bar{t} = 0$, 100, 200, 300, 400. (d) Theoretical and experimental comparison (profilemetry) of dried blood droplet precipitate radial height profile.

blood droplets used in our experiments. Figure 10(a) shows the non-dimensional average concentration profile for various non-dimensional time instants $\bar{t} = 0$, 100, 200, 300, 400. Figure 10(b) shows the evolution of the evaporation flux profile along the drop interface for various non-dimensional time instants $\bar{t} = 0$, 100, 200, 300, 400. The temporal evolution of the average concentration at the outer edge of the droplet depicting sol-gel phase transition (monotonic increase in concentration) is shown in supplementary figure S6. The non-dimensional evaporative flux evolution at the droplet outer edge is also shown in supplementary figure S7 depicting the corresponding monotonic decrease. Figure 10(c) shows the non-dimensional drop height profile as a function of non-dimensional radial coordinate with non-dimensional time as a parameter. Figure 10(d) compares the final dried residue droplet thickness profile with the steady-state theoretical prediction. The theoretical height profile (red dotted line) conforms with the experimental curve obtained from profilometry (black) within the experimental uncertainty. Figure 11(a-g)shows the non-dimensional height profile variation as a function of non-dimensional radial coordinate with non-dimensional time as a parameter in the range $\bar{t} = 0 - 1450$. Figure 11(h) shows the droplet centre height variation as a function of non-dimensional time t/t_* . The theoretical curve in red (labelled as The.) agrees with the experimental observations (labelled as Obs.) within the experimental uncertainty. The variation of

D. Roy and others

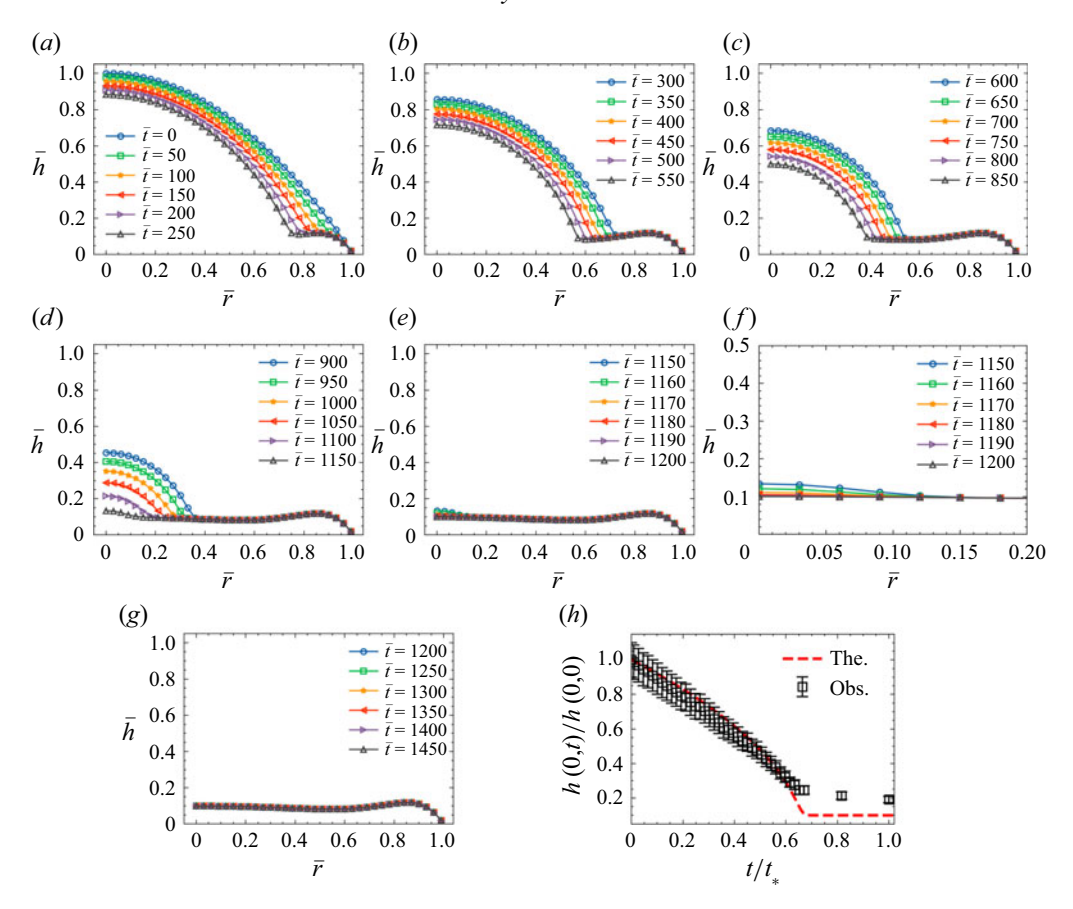


Figure 11. Non-dimensional drop height variation as a function of non-dimensional radial coordinate at various non-dimensional time instants: (a) $\bar{t} = 0-250$; (b) $\bar{t} = 300-550$; (c) $\bar{t} = 600-850$; (d) $\bar{t} = 900-1150$; (e) $\bar{t} = 1150-1200$. (f) Magnified view of non-dimensional height profile near $\bar{r} = 0-0.2$ for time instants: (f) $\bar{t} = 1150-1200$; (g) $\bar{t} = 1200-1450$. (h) Comparison of theoretical and experimental observation of drop centre height variation with time.

the experimental observation from the theoretical prediction after $t/t_* = 0.7$ is due to the fact that the experimental drop centre height data are extracted from the side view. As a result, after the reduction of the central height to approximately a particular value $(h(0, t)/h(0, 0) \sim 0.2)$, further reduction in the central height cannot be measured due to the formation of the thick coronal rim around the droplet. The coronal deposit obstructs the view of the centre part of the droplet causing the measurement to flatten out much earlier compared with the actual theoretical prediction.

3.5. Characterisation of dried blood residues and bacterial distribution

Figure 12(a) shows the SEM image of the dried residue of whole blood drop. The scale bar in white represents 1.3 mm. Various kinds of cracks are generally observed, ranging from radial cracks at the thickest portion to mudflat-type cracks at the drop centre and close to the droplet's outer edge. The cracks result from desiccation stress during the phase transition from wet to dry gel. Cracks, in general, intersect each other either at right angles or 120°. The resulting cracks fragment the dried residue into several flakes. Figure 12(b) shows the radial size distribution of the flakes for a typical dried residue

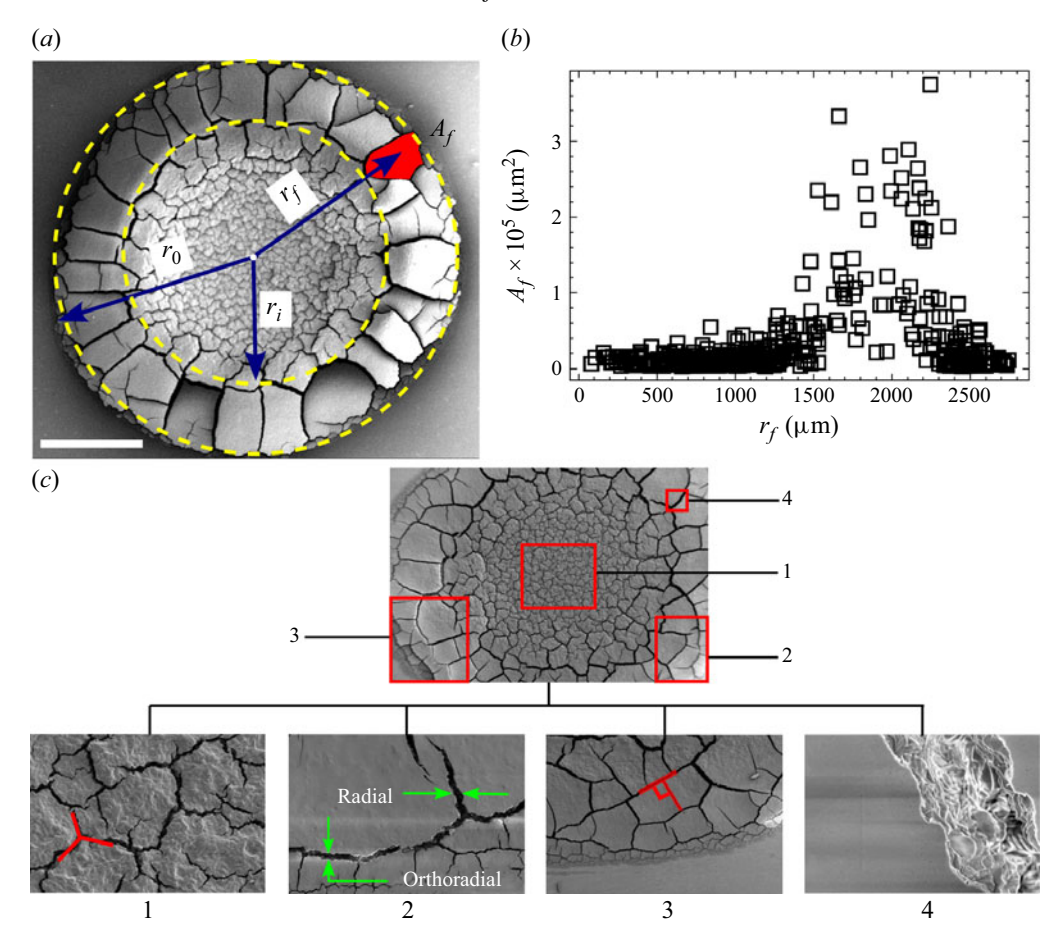


Figure 12. Dried blood precipitate characterisation using (a) SEM denoting various kinds of cracks and flakes. Scale bar represents 1.3 mm. (b) Radial flake size distribution of dried whole blood drop residue. (c) Cracks characterisation in dried whole blood precipitate. The numerals 1–4 represents different viewing region of interest (ROI). Regions 1, 2, 3, 4 represent the centre, outer edge of the central region, peripheral region (corona) and a radial crack, respectively.

of contact radius R=2.7 mm. Here, A_f denotes the area of a particular flake with a radial centroid coordinate r_f and R denotes the drop contact radius. The flake size is highest between $r_f=1600$ and 2300 μ m, i.e. in the peripheral region ($r_i=1600$ μ m, $r_0=2300$ μ m). The flake size is smaller in the drop centre and the outer edge of the droplet. Various regions of the dried residue can be characterised following Brutin *et al.* (2011). The region $0 < r < r_i$ refers to the central area of the drop, and the residue pattern is formed due to wetting deposits in general. The region $r_i < r < r_0$ forms the outer rim region called the corona. The deposition in the corona region is majorly due to the radially outward transport of RBCs due to the capillary flow inside the evaporating droplet. The outermost region $r_0 < r < R$ near the contact line of the drop has a deposit structure and crack morphology similar to the drop centre formed due to wetting deposit. Figure 12(c) depicts the various cracks formed due to desiccation stress while transforming from wet gel to dry gel in stage C of blood drop evaporation. Different regions of interest in the dried residue are shown in red rectangles and labelled with numerals 1–4. The central region labelled as 1 generally has mud-flat-type cracks. The cracks in the central region

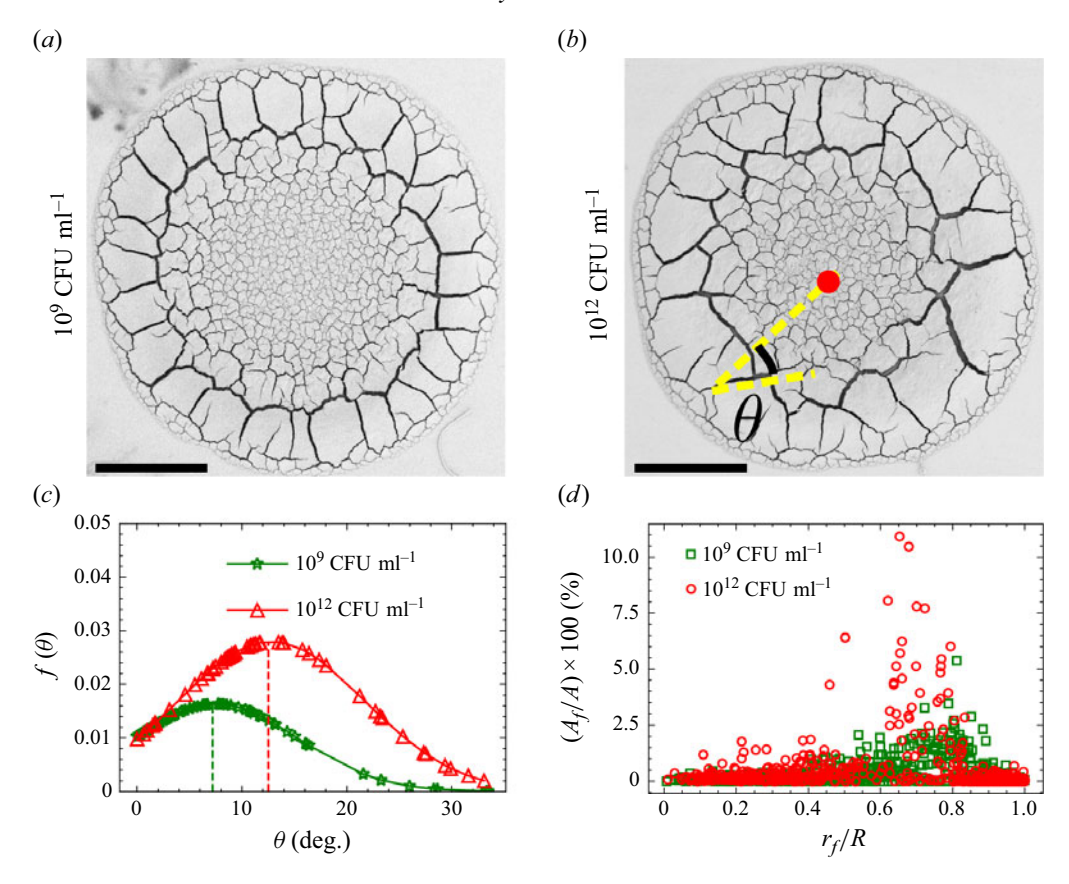


Figure 13. Comparison of final precipitate pattern using SEM for (a) 10^9 CFU ml⁻¹ and (b) 10^{12} CFU ml⁻¹. The angle θ measures the deviation from a radial crack. (c) Probability density function $f(\theta)$ of the crack angle for 10^9 CFU ml⁻¹ and 10^{12} CFU ml⁻¹. (d) Radial distribution of flake size represented as an area fraction/percentage for 10^9 CFU ml⁻¹ and 10^{12} CFU ml⁻¹.

are typically shaped like 'Y' at a vertex (intersection of cracks). Further, the cracks at a 'Y' vertex typically subtend approximately equal angles close to 120° (figure 12c-1). The cracks in the corona region labelled as 2 and 3 are typically 'T' shaped and rectilinear. The cracks generally are radial and orthoradial (figure 12 c-2), intersecting at a right angle at the particular vertex (figure 12c-3). The crack pattern of whole blood is drastically different from the crack pattern formed in pure blood plasma. Refer to supplementary figure S8 for the various types of cracks formed in evaporating a pure plasma drop. Figures 13(a) and 13(b) depicts the final precipitate for 10^9 CFU ml⁻¹ and 10^{12} CFU ml^{-1} , respectively, using SEM. Figure 13(c) shows the probability density function (p.d.f.) $f(\theta)$ for the angle of deviation θ (refer to figure 13b) from the radial direction. The angle θ defined in figure 13(b) measures the degree a crack deviates from the radial direction. From figure 13(c), it is clearly evident that the crack patterns in the peripheral corona region of the droplet deviate in the radial direction significantly for relatively higher bacterial concentration in comparison to lower bacterial concentration. Figure 13(d) shows the radial distribution of flake size represented as an area fraction/percentage for the whole droplet precipitate for 10⁹ CFU ml⁻¹ and 10¹² CFU ml⁻¹. Further, it is also evident from figure 13(d) that the coronal flake sizes are relatively larger for 10^{12} CFU ml⁻¹ bacterial concentration in comparison with those at 10⁹ CFU ml⁻¹. Figure 14 depicts a typical

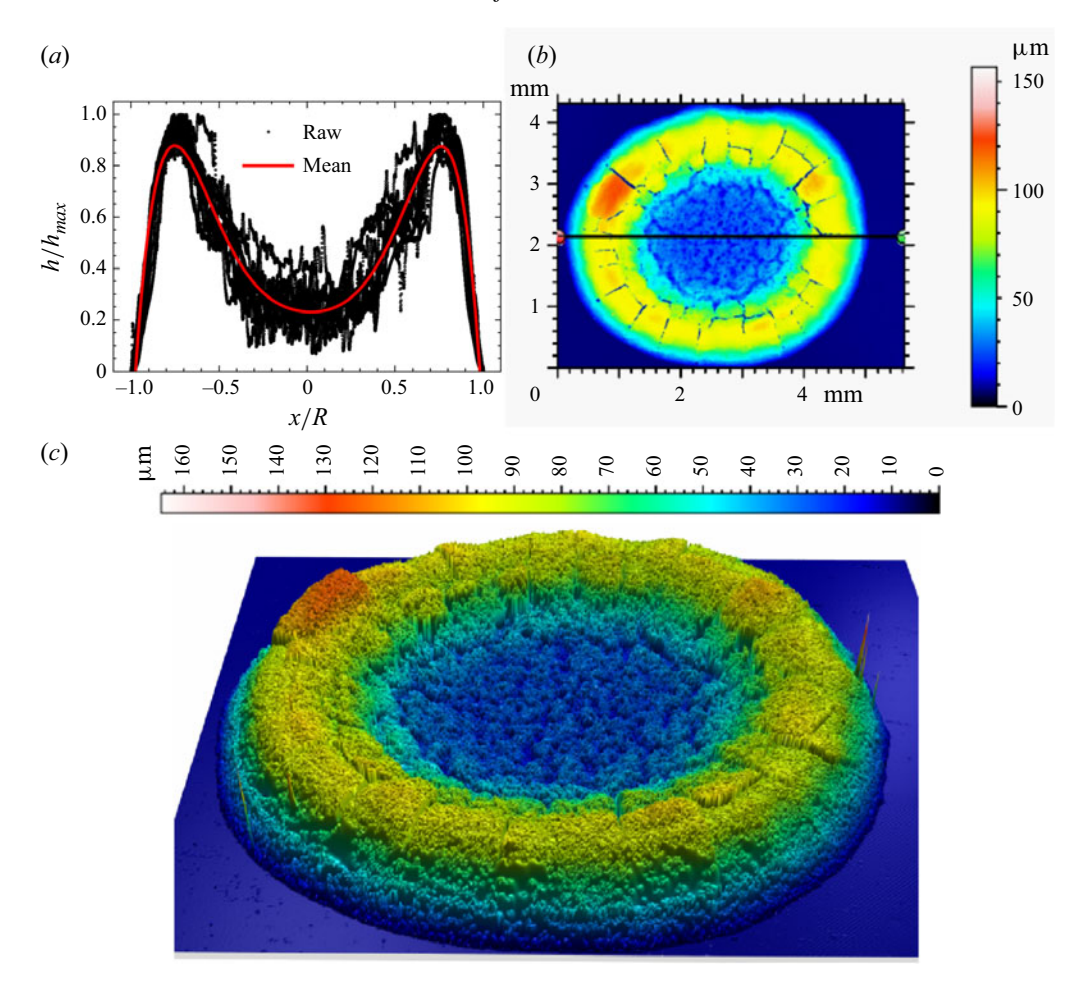


Figure 14. Dried blood drop surface thickness characterisation using optical profilometry. (a) One-dimensional surface profile thickness variation along the horizontal diametric axis (shown as black line in panel b) of the dried blood droplet precipitate. The black dots represents raw profilometry data as a function of radial coordinate. The red solid curve denotes the mean thickness profile. (b) Two-dimensional visualisation of dried precipitate surface thickness represented as a filled contour plot. (c) Three-dimensional perspective visualisation of the dried residue surface and its corresponding thickness.

microcharacterisation of the dried residue of whole blood using optical profilometry. Figure 14(a) shows the one-dimensional (1-D) thickness profile along the section shown by a black horizontal line (figure 14b) passing through the drop diameter. The black dots represent the raw profilometry normalised height data and the red curve is the normalised mean thickness profile of the droplet. Figure 14(b) depicts the 2-D thickness profile filled-contour. Figure 14(c) depicts a 3-D visualisation of the surface thickness profile for the dried blood precipitate. Note that the thickness of the dried precipitate is the smallest at the drop centre and the outer contact line of the droplet. We observe that the crack thickness, length and flake size at any given position are proportional to the thickness of the dried residue. Therefore, regions with higher thickness will have larger crack lengths and flake sizes. Physically, the crack length represents a scale over which the cracks form and stresses relax (Goehring 2013). We also observe that bacteria-laden blood droplets do not show a significant difference in terms of evaporation and dried

residue characteristics from pure whole blood droplets within the concentration range typically found in living organisms $\sim < (10^9)$ CFU ml⁻¹ (refer to figure 2b). The negligible difference in drop evaporation and dried residue characteristics is probably due to RBCs being one order of magnitude ($\sim \mathcal{O}(10)$) bigger in length scale and hence approximately two orders ($\sim \mathcal{O}(10^2)$) larger in terms of area ratio. The maximum bacterial concentration of 10⁹ CFU ml⁻¹ will give approximately similar number density as RBCs. However, owing to the area ratio, the bacteria will be uniformly distributed throughout the plasma protein matrix with the highest fraction embedded and packed between the biconcave curvatures of the RBCs. For bacteria to have appreciable effects in the corresponding evaporation physics, the bacterial number density has to be significantly altered by the presence of bacteria. Alteration of bacterial number density is only possible at very high bacterial concentrations ($c \sim 10^{12}$ CFU ml⁻¹). From figure 2(b), we observe that 10^{12} CFU ml⁻¹ reduces the evaporation rate in comparsion to lower bacteria concentration. This reduction in evaporation rate causes flake size to be larger compared with at high evaporation rate (Zeid, Vicente & Brutin 2013). At these extreme concentrations of 10¹² CFU ml⁻¹, the crack pattern in the corona region deviates significantly from that found in lower concentrations (refer to figures 2d, 13a and 13b for the difference in crack patterns). Figures 15(a) and 15(b) depict the bacterial deposition in the dried residue of blood plasma and whole blood droplets using confocal fluorescence microscopy. The scale bar in white denotes 500 μ m. Figure 15(c-e) shows the RBCs' shape, deposition and stacking in the dried blood residue using SEM. Generally, the RBCs stack in columnar structures known as rouleaux due to Smoluchowski aggregation/coagulation kinetics (Samsel & Perelson 1982, 1984; Barshtein, Wajnblum & Yedgar 2000). Due to the evaporation of blood droplets, the solute concentration increases. As a result, blood tonicity changes from isotonic to hypertonic, causing the RBCs to shrink in size due to water transport out of the red cells, as shown schematically in figure 15(f). The water transport outside the RBCs is caused by the osmotic pressure gradient, resulting in shrunken and wrinkled RBCs inside the precipitate of the evaporating droplet. Pal et al. (2020) speculate that the wrinkled structures are deformed WBCs. However, owing to the very high number concentration in comparison to WBCs and platelets, the authors show that the dominant processes and structure formation that occur during blood droplet evaporation is due to the transport and deposition of RBCs. The ridge-like structures are deformed RBCs that form during osmosis as explained previously. This could also be understood by looking at the relevant length scales involved. It is evident from figure 15(c-f) that the ridge-like structures form on top of surfaces which are well structured and have dimensions/length scales similar to RBCs. Also, such structures are found in Rouleax stacks which are a well-known signature of RBCs stacking. WBCs in general are bigger than RBCs and also do not have a smooth spherical shape. Further, WBCs do not show Rouleax kind of stack formation and hence eliminates the possibility of the ridge-like structures to be deformed WBCs. Platelets are one order smaller than RBCs and hence cannot be related to the ridgelike structures as the structures are seen on objects having length scales similar to RBCs. The distribution of bacteria in the dried blood residue for 10^6 CFU ml⁻¹, 10^9 CFU ml⁻¹ and 10^{12} CFU ml⁻¹ can be seen from confocal microscopy images shown in figure 16(a). Figures 16(b) and 16(c) show fluorescent tagged bacterial path lines from live confocal microscopy at the outer edge and the central region of the evaporating droplet for 10¹² CFU ml⁻¹ bacterial concentration. Refer to supplementary movies 4–9 to visualise the radially outward bacterial motion for various different bacterial concentrations and regions of interest (drop edge and the centre).

It is clear from figure 16 that the bacteria moves approximately radially outwards on average towards the pinned contact line due to the internal capillary flow generated inside

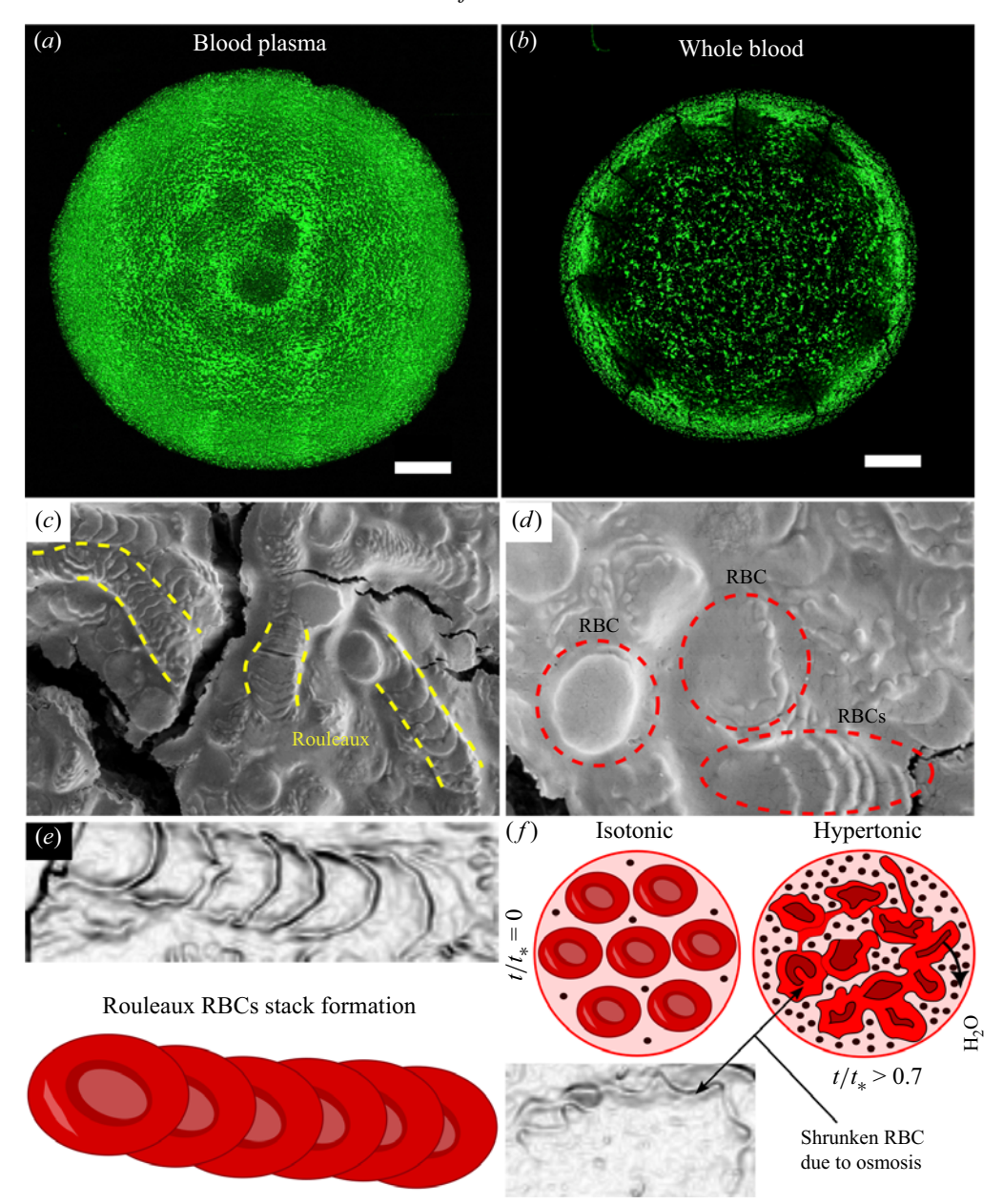


Figure 15. Confocal fluroscence microscopy images depicting bacterial distribution in the dried precipitate of (a) blood plasma and (b) whole blood droplet. The white scale bar represents 500 μ m. (c) SEM image depicting RBCs distribution in the dried blood precipitate. (d) SEM image depicting shrunken RBCs. (e) Schematic representation of Rouleaux stack formation of RBCs. (f) Schematic representing osmosis in RBCs causing shape deformation from biconcave disk to shrunken state at the end state of evaporation (stage C).

the evaporating droplet. This is also evident from the radially outward bacterial path lines shown in figures 16(b) and 16(c). The actual local trajectory of the individual bacteria are curvilinear and very complex in general as they travel through a multicomponent phase consisting of various cellular components and plasma (refer to supplementary figure S9). The individual trajectories of the bacteria are clearly visible from the live confocal imaging

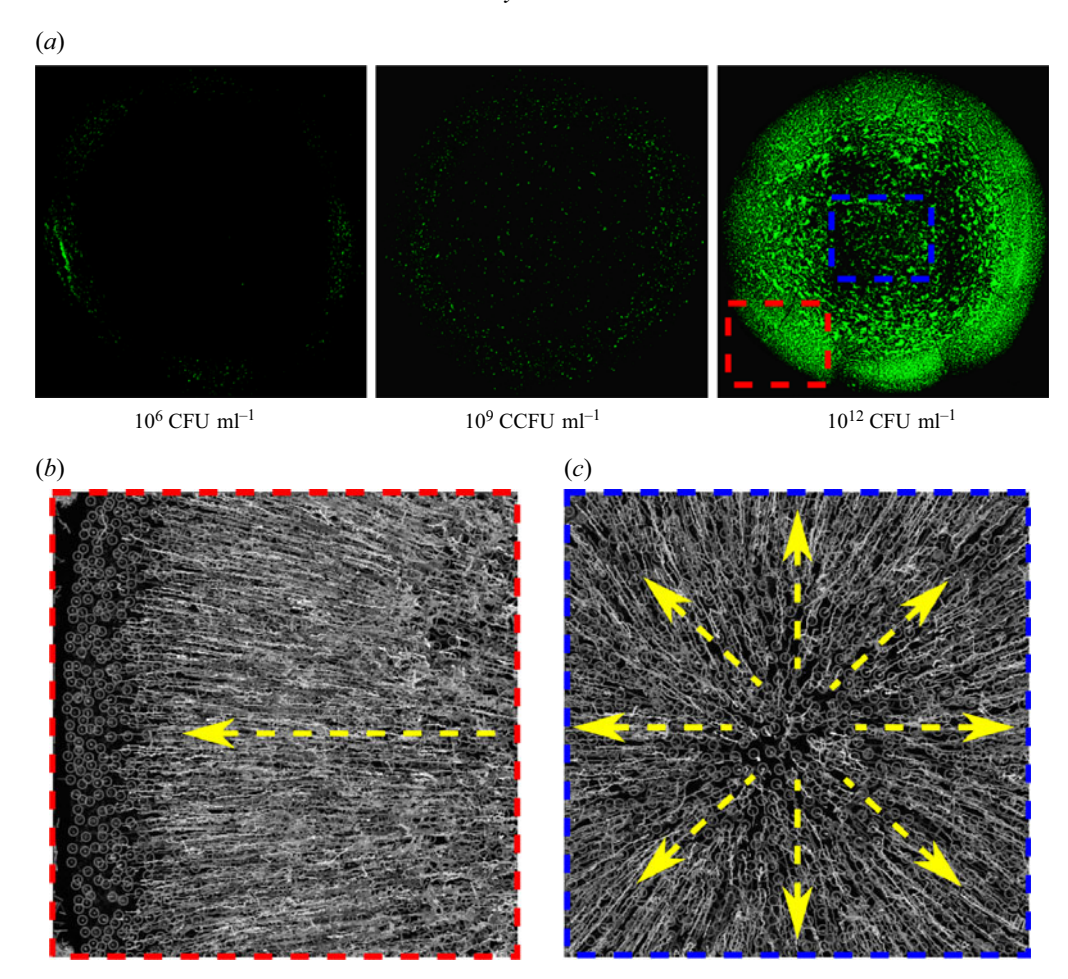


Figure 16. (a) Confocal microscopy images depicting the final bacterial deposit pattern for 10^6 CFU ml⁻¹, 10^9 CFU ml⁻¹ and 10^{12} CFU ml⁻¹. (b) Radially outward pathlines of bacteria at the outer edge of the evaporating droplet (refer to red dotted rectangle in panel a) for 10^{12} CFU ml⁻¹. (c) Radially outward pathlines of bacteria at the centre of the evaporating droplet (refer to blue dotted rectangle in panel a) for 10^{12} CFU ml⁻¹.

(refer to supplementary movies 6 and 7). The actual local deposition of the bacteria in the final blood precipitate depends on the superposition of the outward radial capillary flow in conjunction to the local perturbation of the bacterial trajectories caused due to the presence of cellular and protein components. The highly irregular cracks in the coronal region for very high bacterial concentration is probably related to the thread-like bacterial trajectories that get packed in the final dry-gel precipitate. A thorough understanding of the microphysics and the corresponding fluid dynamics is beyond the scope of the current study and shall be taken as a future endeavour.

4. Conclusion

In conclusion, we study the mechanics of sessile whole blood drop evaporation using direct experimental visualisation and theoretical methods like time sequence analysis, lubrication analysis and micro/nano-characterisation. We identified that blood drop evaporation, in general, can be subdivided into three stages (A, B, C) based on the evaporation rate.

Stage A is the fastest and consists of the gelation of the contact line due to the radial transport of RBCs caused by the outward capillary flow. The gelation occurs due to solgel phase transition. Stage B consists of an intermediate evaporation rate in which the gelation front moves radially inward. The radially inward gelation front propagation and droplet height reduction cause the phase transition of the entire droplet into a wet-gel state. The wet-gel phase changes to a dry-gel state in stage C of droplet evaporation. Further, we show that the precipitate thickness profile computed from the theoretical analysis conforms to the optical profilometry measurements. We also observe lamination to delamination transition in stage C, which provides quantitative data on the slowest stage C of evaporation. Further, as the wet gel transitions to dry gel, the final dried residue precipitate undergoes desiccation-induced stresses that lead to different kinds of cracks forming on the precipitate. The crack characteristics depend highly on the precipitate's local thickness; hence, a one-to-one map exists between precipitate thickness and the corresponding cracks that are formed. We further show that the drop evaporation rate and final dried precipitate pattern do not change appreciably within the parameter variation of the bacterial concentration ($c \le 10^9$ CFU ml⁻¹) typically found in bacterial infection of living organisms. However, at very high bacterial concentration ($c \sim 10^{12} \text{ CFU ml}^{-1}$), which is biologically not feasible for a living organism, we observe the cracks formed in the coronal region of the precipitate deviate from the typical radial cracks found in lower concentrations.

Supplementary materials and movies. Supplementary materials and movies are available at https://doi.org/10.1017/jfm.2025.10720.

Acknowledgements. The authors acknowledge and thank Navin Kumar Chandra for helping with the viscosity measurements of the blood samples.

Declaration of interests. The authors declare no conflict of interest.

REFERENCES

- ADACHI, E., DIMITROV, A.S. & NAGAYAMA, K. 1995 Stripe patterns formed on a glass surface during droplet evaporation. *Langmuir* 11 (4), 1057–1060.
- AGHARKAR, A.N., HAJRA, D., ROY, D., JAISWAL, V., KABI, P., CHAKRAVORTTY, D. & BASU, S. 2024 Evaporation of bacteria-laden surrogate respiratory fluid droplets: on a hydrophilic substrate vs contact-free environment confers differential bacterial infectivity. *Phys. Fluids* **36** (3), 031912.
- ALLAIN, C. & LIMAT, L. 1995 Regular patterns of cracks formed by directional drying of a collodial suspension. *Phys. Rev. Lett.* **74** (15), 2981.
- ANDERSON, D.M. & DAVIS, S.H. 1995 The spreading of volatile liquid droplets on heated surfaces. *Phys. Fluids* 7 (2), 248–265.
- BAHMANI, L., NEYSARI, M. & MALEKI, M. 2017 The study of drying and pattern formation of whole human blood drops and the effect of thalassaemia and neonatal jaundice on the patterns. *Colloid. Surfaces A: Physicochem. Enging Aspects* **513**, 66–75.
- BARSHTEIN, G., WAJNBLUM, D. & YEDGAR, S. 2000 Kinetics of linear rouleaux formation studied by visual monitoring of red cell dynamic organization. *Biophys. J.* **78** (5), 2470–2474.
- BASKURT, O.K. & MEISELMAN, H.J. 2003 Blood rheology and hemodynamics. In *Seminars in Thrombosis* and *Hemostasis*, vol. 29, pp. 435–450, Copyright© 2003 by Thieme Medical Publishers, Inc., 333 Seventh Avenue, New.
- BENABDELHALIM, H. & BRUTIN, D. 2022 Drying of human blood drops.
- BERGEL, D.H. 2012 Cardiovascular Fluid Dynamics. Elsevier.
- BHARDWAJ, R., FANG, X. & ATTINGER, D. 2009 Pattern formation during the evaporation of a colloidal nanoliter drop: a numerical and experimental study. *New J. Phys.* 11 (7), 075020.
- BHARDWAJ, R., FANG, X., SOMASUNDARAN, P. & ATTINGER, D. 2010 Self-assembly of colloidal particles from evaporating droplets: role of dlvo interactions and proposition of a phase diagram. *Langmuir* **26** (11), 7833–7842.
- BLOSSEY, R. & BOSIO, A. 2002 Contact line deposits on cdna microarrays: a 'twin-spot effect'. *Langmuir* 18 (7), 2952–2954.

D. Roy and others

- BODIGUEL, H. & LENG, J. 2010 Imaging the drying of a colloidal suspension. Soft Matter 6 (21), 5451-5460.
- BRUTIN, D. 2015 Droplet Wetting and Evaporation: From Pure to Complex Fluids. Academic Press.
- Brutin, D. & Sefiane, K. 2022 Drying of complex fluid drops. In *Fundamentals and Applications*, vol. 14, Royal Society of Chemistry.
- BRUTIN, D., SOBAC, B., LOQUET, B. & SAMPOL, J. 2011 Pattern formation in drying drops of blood. *J. Fluid Mech.* 667, 85–95.
- Brutin, D. & Starov, V. 2018 Recent advances in droplet wetting and evaporation. *Chem. Soc. Rev.* 47 (2), 558–585.
- CAMERON, J.M., BUTLER, H.J., PALMER, D.S. & BAKER, M.J. 2018 Biofluid spectroscopic disease diagnostics: a review on the processes and spectral impact of drying. *J. Biophotonics* 11 (4), e201700299.
- CHEN, R., ZHANG, L., ZANG, D. & SHEN, W. 2016 Blood drop patterns: formation and applications. *Adv. Colloid Interface Sci.* 231, 1–14.
- CHOI, J., KIM, W. & KIM, H.-Y. 2020 Crack density in bloodstains. Soft Matter 16 (24), 5571-5576.
- CLIFT, R., GRACE, J.R. & WEBER, M.E. 2005 Bubbles, drops, and particles.
- D'AMBROSIO, H.-M., WILSON, S.K., WRAY, A.W. & DUFFY, B.R. 2023 The effect of the spatial variation of the evaporative flux on the deposition from a thin sessile droplet. *J. Fluid Mech.* **970**, A1.
- DEEGAN, R.D., BAKAJIN, O., DUPONT, T.F., HUBER, G., NAGEL, S.R. & WITTEN, T.A. 1997 Capillary flow as the cause of ring stains from dried liquid drops. *Nature* **389** (6653), 827–829.
- DEEGAN, R.D., BAKAJIN, O., DUPONT, T.F., HUBER, G., NAGEL, S.R. & WITTEN, T.A. 2000 Contact line deposits in an evaporating drop. *Phys. Rev. E* 62 (1), 756.
- DEMIR, R., et al. 2024 Artificial intelligence assisted patient blood and urine droplet pattern analysis for non-invasive and accurate diagnosis of bladder cancer. Sci. Rep.-UK 14 (1), 2488.
- DENKOV, N., VELEV, O., KRALCHEVSKI, P., IVANOV, I., YOSHIMURA, H. & NAGAYAMA, K. 1992 Mechanism of formation of two-dimensional crystals from latex particles on substrates. *Langmuir* 8 (12), 3183–3190.
- DU, F., ZHANG, L. & SHEN, W. 2022 The internal flow in an evaporating human blood plasma drop. J. Colloid Interface Sci. 609, 170–178.
- Dufresne, E.R., Corwin, E.I., Greenblatt, N.A., Ashmore, J., Wang, D.Y., Dinsmore, A.D., Cheng, J.X., Xie, X.S., Hutchinson, J.W. & Weitz, D.A. 2003 Flow and fracture in drying nanoparticle suspensions. *Phys. Rev. Lett.* **91** (22), 224501.
- DUGAS, V., BROUTIN, J. & SOUTEYRAND, E. 2005 Droplet evaporation study applied to dna chip manufacturing. *Langmuir* 21 (20), 9130–9136.
- ERSHOV, D., et al. 2022 TrackMate 7: integrating state-of-the-art segmentation algorithms into tracking pipelines. *Nat. Meth.* **19** (7), 829–832.
- ESMONDE-WHITE, K.A., ESMONDE-WHITE, F.W.L., MORRIS, M.D. & ROESSLER, B.J. 2014 Characterization of biofluids prepared by sessile drop formation. *Analyst* 139 (11), 2734–2741.
- FISCHER, B.J. 2002 Particle convection in an evaporating colloidal droplet. Langmuir 18 (1), 60-67.
- GENNES, P.-G., BROCHARD-WYART, F., QUÉRÉ, D. & et al. 2004 Capillarity and Wetting Phenomena: Drops, Bubbles, Pearls, Waves. Springer.
- GOEHRING, L. 2013 Evolving fracture patterns: columnar joints, mud cracks and polygonal terrain. *Phil. Trans. R. Soc. A: Math., Phys. Engng Sci.* **371**(2004), 20120353
- HERTAEG, M.J., TABOR, R.F., ROUTH, A.F. & GARNIER, G. 2021 Pattern formation in drying blood drops. Phil. Trans. R. Soc. A 379 (2203), 20200391.
- HOFFBRAND, V. & STEENSMA, D.P. 2019 Hoffbrand's Essential Haematology. John Wiley & Sons.
- Hu, H. & Larson, R.G. 2002 Evaporation of a sessile droplet on a substrate. J. Phys. Chem. B 106 (6), 1334–1344.
- HU, H. & LARSON, R.G. 2005 Analysis of the microfluid flow in an evaporating sessile droplet. *Langmuir* 21 (9), 3963–3971.
- HULSE-SMITH, L., MEHDIZADEH, N.Z. & CHANDRA, S. 2005 Deducing drop size and impact velocity from circular bloodstains. *J. Forensic Sci.* **50** (1), JFS2003224–10.
- IQBAL, R., SHEN, AMY Q. & SEN, A.K. 2020 Understanding of the role of dilution on evaporative deposition patterns of blood droplets over hydrophilic and hydrophobic substrates. J. Colloid Interface Sci. 579, 541–550.
- ISRAELACHVILI, J.N. 2011 Intermolecular and Surface Forces. Academic press.
- JUNG, Y., KAJIYA, T., YAMAUE, T. & DOI, M. 2009 Film formation kinetics in the drying process of polymer solution enclosed by bank. *Japan. J. Appl. Phys.* 48 (3R), 031502.
- KAPLAN, C.N. & MAHADEVAN, L. 2015 Evaporation-driven ring and film deposition from colloidal droplets. J. Fluid Mech. 781, R2.

- KOKORNACZYK, M.O., BODROVA, N.B. & BAUMGARTNER, S. 2021 Diagnostic tests based on pattern formation in drying body fluids A mapping review. *Colloid. Surf. B: Biointerfaces* **208**, 112092.
- KOOYMAN, B., NEWMAN, M.E. & CERI, H. 1992 Verifying the reliability of blood residue analysis on archaeological tools. *J. Archaeol. Sci.* 19 (3), 265–269.
- LANOTTE, L., LAUX, D., CHARLOT, B. & ABKARIAN, M. 2017 Role of red cells and plasma composition on blood sessile droplet evaporation. *Phys. Rev. E* **96** (5), 053114.
- LAUX, D., FERRANDIS, J. Y. & BRUTIN, D. 2016 Ultrasonic monitoring of droplets' evaporation: application to human whole blood. *Ultrason. Sonochem.* **32**, 132–136.
- WAITE, L., et al. 2007 Applied Biofluid Mechanics. The McGraw-Hill Medical Companies, Inc.
- MOORE, M.R., VELLA, D. & OLIVER, J.M. 2021 The nascent coffee ring: how solute diffusion counters advection. *J. Fluid Mech.* **920**, A54.
- MOORE, M.R., VELLA, D. & OLIVER, J.M. 2022 The nascent coffee ring with arbitrary droplet contact set: an asymptotic analysis. *J. Fluid Mech.* **940**, A38.
- MOORE, M.R. & WRAY, A.W. 2023 Gravitational effects on coffee-ring formation during the evaporation of sessile droplets. J. Fluid Mech. 967, A26.
- MUKHOPADHYAY, M., RAY, R., AYUSHMAN, M., SOOD, P., BHATTACHARYYA, M., SARKAR, D. & DASGUPTA, S. 2020 Interfacial energy driven distinctive pattern formation during the drying of blood droplets. *J. Colloid Interface Sci.* 573, 307–316.
- NGUYEN, V.X. & STEBE, K.J. 2002 Patterning of small particles by a surfactant-enhanced marangoni-bénard instability. *Phys. Rev. Lett.* **88** (16), 164501.
- OKUZONO, T., AOKI, N., KAJIYA, T. & DOI, M. 2010 Effects of gelation on the evaporation rate of polymer solutions. *J. Phys. Soc. Japan* **79** (9), 094801.
- PAL, A., GOPE, A. & IANNACCHIONE, G. 2021 Temperature and concentration dependence of human whole blood and protein drying droplets. *Biomolecules* 11 (2), 231.
- PAL, A., GOPE, A., OBAYEMI, J.D. & IANNACCHIONE, G.S. 2020 Concentration-driven phase transition and self-assembly in drying droplets of diluting whole blood. *Sci. Rep.-UK* 10 (1), 18908.
- PAL, A., GOPE, A. & SENGUPTA, A. 2023 Drying of bio-colloidal sessile droplets: advances, applications, and perspectives. Adv. Colloid Interface Sci. 314, 102870.
- REINHART, W.H. 2016 The optimum hematocrit. Clin. Hemorheol. Micro. 64 (4), 575-585.
- ROY, D. & BASU, S. 2024 Future research perspective on the interfacial physics of non-invasive glaucoma testing in pathogen transmission from the eyes. *Biointerphases* **19** (1), 018501.
- ROY, D., PANDEY, K., BANIK, M., MUKHERJEE, R. & BASU, S. 2019 Dynamics of droplet impingement on bioinspired surface: insights into spreading, anomalous stickiness and break-up. *Proc. R. Soc. A* 475 (2229), 20190260.
- ROY, D., SOPHIA, M., RAO, S.S. & BASU, S. 2022 Droplet impact on immiscible liquid pool: multi-scale dynamics of entrapped air cushion at short timescales. *Phys. Fluids* 34 (5), 052004.
- ROY, D., SOPHIA, M. & BASU, S. 2023 On the mechanics of droplet surface crater during impact on immiscible viscous liquid pool. J. Fluid Mech. 955, A27.
- SADHAL, S.S., AYYASWAMY, P.S. & CHUNG, J.N. 2012 Transport Phenomena with Drops and Bubbles. Springer Science & Business Media.
- SAMSEL, R.W. & PERELSON, A.S. 1984 Kinetics of rouleau formation. II. Reversible reactions. *Biophys. J.* 45 (4), 805–824.
- SAMSEL, R.W. & PERELSON, A.S. 1982 Kinetics of rouleau formation. i. a mass action approach with geometric features. *Biophys. J.* 37 (2), 493–514.
- SCHNEIDER, C.A., RASBAND, W.S. & ELICEIRI, K.W. 2012 Nih image to imagej: 25 years of image analysis. *Nat. Meth.* **9** (7), 671–675.
- SEYFERT, C., RODRÍGUEZ-RODRÍGUEZ, J., LOHSE, D. & MARIN, A. 2022 Stability of respiratory-like droplets under evaporation. *Phys. Rev. Fluids* 7 (2), 023603.
- SHATOKHINA, S.N., et al. 2004 Bio-liquid morphological analysis. Scientific World J. 4, 657–661.
- SMALYUKH, I.I., ZRIBI, O.V., BUTLER, J.C., LAVRENTOVICH, O.D. & WONG, G.C.L. 2006 Structure and dynamics of liquid crystalline pattern formation in drying droplets of dna. *Phys. Rev. Lett.* 96 (17), 177801.
- SOBAC, B. & BRUTIN, D. 2011 Structural and evaporative evolutions in desiccating sessile drops of blood. *Phys. Rev. E* **84** (1), 011603.
- SOBAC, B. & BRUTIN, D. 2014 Desiccation of a sessile drop of blood: cracks, folds formation and delamination. *Colloid. Surf. A: Physicochem. Engng Aspects* 448, 34–44.
- STAUBER, J.M., WILSON, S.K., DUFFY, B.R. & SEFIANE, K. 2014 On the lifetimes of evaporating droplets. J. Fluid Mech. 744, R2.
- SULTAN, E., BOUDAOUD, A. & AMAR, M.B. 2005 Evaporation of a thin film: diffusion of the vapour and Marangoni instabilities. *J. Fluid Mech.* **543**, 183–202.

D. Roy and others

- TARASEVICH, Y.Y., VODOLAZSKAYA, I.V. & ISAKOVA, O.P. 2011 Desiccating colloidal sessile drop: dynamics of shape and concentration. *Colloid Polym. Sci.* 289, 1015–1023.
- TINEVEZ, J.-Y., PERRY, N., SCHINDELIN, J., HOOPES, G.M., REYNOLDS, G.D., LAPLANTINE, E., BEDNAREK, S.Y., SHORTE, S.L. & ELICEIRI, K.W. 2017 Trackmate: an open and extensible platform for single-particle tracking. *Methods* 115, 80–90.
- Traipe-Castro, L., Salinas-Toro, D., López, D., Zanolli, M., Srur, M., Valenzuela, F., Cáceres, A., Toledo-Araya, H. & López-Solís, R. 2014 Dynamics of tear fluid desiccation on a glass surface: a contribution to tear quality assessment. *Biol. Res.* 47, 1–10.
- Trantum, J.R., Wright, D.W. & Haselton, F.R. 2012 Biomarker-mediated disruption of coffee-ring formation as a low resource diagnostic indicator. *Langmuir* 28 (4), 2187–2193.
- VAN ROSSUM, G. & DRAKE, F.L. 2009 Python 3 reference manual createspace. Scotts Valley, CA..
- WILKING, J.N., ZABURDAEV, V., DE, V., MICHAEL, L., RICHARD, B., MICHAEL, P. & WEITZ, D.A. 2013 Liquid transport facilitated by channels in bacillus subtilis biofilms. *Proc. Natil Acad. Sci.* 110 (3), 848–852.
- WILSON, A.S., et al. 2013 Archaeological, radiological, and biological evidence offer insight into Inca child sacrifice. Proc. Natl Acad. Sci. 110 (33), 13322–13327.
- WILSON, S.K. & D'AMBROSIO, H.-M. 2023 Evaporation of sessile droplets. *Annu. Rev. Fluid Mech.* 55, 481–509.
- YAKHNO, T.A., SANIN, A.G., YAKHNO, V.G., PELYUSHENKO, A.S., DOWELL, M.B., VACCA, C. & GOUTOROVA, V.A. 2005 Drying drops of biological liquids: dynamics of the optical and mechanical properties. application in rapid medical diagnostics. In *Advanced Biomedical and Clinical Diagnostic Systems III*, vol. 5692, pp. 188–198. SPIE.
- YARIN, A.L., ROISMAN, I.V. & TROPEA, C. 2017 Collision Phenomena in Liquids and Solids. Cambridge University Press.
- ZEID, W.B., VICENTE, J. & BRUTIN, D. 2013 Influence of evaporation rate on cracks' formation of a drying drop of whole blood. *Colloid. Surf. A: Physicochem. Engng Aspects* **432**, 139–146.